AIAA JOURNAL
Vol. 49, No. 8, August 2011

Parameter-Free Simple Low-Dissipation AUSM-Family Scheme for All Speeds

Eiji Shima* and Keiichi Kitamura†
Japan Aerospace Exploration Agency, Sagamihara 252-5210, Japan

DOI: 10.2514/1.J050905

This paper presents a new, simple low-dissipation numerical flux function of the AUSM-family for all speeds, called the simple low-dissipation AUSM. In contrast with existing all-speed schemes, the simple low-dissipation AUSM features low dissipation without any tunable parameters in a low Mach number regime while it keeps the robustness of the AUSM-family fluxes against shock-induced anomalies at high Mach numbers (e.g., carbuncle phenomena). Furthermore, the simple low-dissipation AUSM has a simpler formulation than the other all-speed schemes. These advantages of the present scheme are demonstrated in numerical examples of a wide spectrum of Mach numbers.

Nomenclature

A	=	wave amplitude
C	=	chord length of airfoil
c	=	sound speed
e	=	total energy of unit volume
f_p	=	numerical dissipation function of M in pressure flux in proposed scheme
f_ρ	=	numerical dissipation function of M in mass flux in proposed scheme
$\tilde{\mathbf{F}}_{i,j}$, $\tilde{\mathbf{R}}_{i,j}$	=	inviscid and viscous flux vectors from ith to jth cells
g	=	switching function of M in proposed scheme for strong expansion cases
h	=	total enthalpy
l	=	wavelength
M	=	Mach number
$\dot{m}$	=	mass flux, $\dot{m} = \rho u$
Pr	=	Prandtl number, 0.72
p	=	pressure
$\tilde{p}$	=	pressure flux
q	=	primitive variables
$\mathbf{Q}_i$	=	conservative variables of cell i
R	=	radius of circular cylinder
Re	=	Reynolds number
St	=	Strouhal number
$s_{i,j}$	=	interface area of cells i and j
u, v, w	=	velocity components in Cartesian coordinates
V_i	=	volume of cell i
V_n	=	velocity component normal to cell interface
x_n, y_n, z_n	=	normal vector components in Cartesian coordinates
β	=	coefficient in AUSM+ and AUSM$^+$-up, 1/8
β_+, β_-	=	function of M in AUSM-family schemes
Γ	=	preconditioning matrix
γ	=	specific heat ratio, 1.4
ε	=	preconditioning coefficient, or decay ratio of wave amplitude
κ	=	thermal conductivity
μ	=	(molecular) viscosity
ρ	=	density
χ	=	switching function in proposed scheme

Subscripts

L, R	=	left and right running wave components
o	=	cutoff in AUSM$^+$-up scheme
t	=	turbulent
0	=	initial or stagnation value
1/2	=	cell-interfacial value
∞	=	freestream value

Superscripts

$+$	=	left-side value at cell interface
$-$	=	right-side value at cell interface
$\bar{\ }$	=	averaged value of both sides at cell interface

I. Introduction

WHEN we attempt to apply compressible computational fluid dynamics (CFD) methods to very low Mach number flows, as is known, we shall pay particular attention to slow, or sometimes stalled, convergence due to the huge ratio of characteristic speeds and the errors arising from an excessive amount of numerical dissipation. These defects are dramatically overcome by using preconditioning matrix methods [1–3]. These methods work well under a subsonic speed; however, shortcomings of the original (unpreconditioned) schemes in higher Mach number flows are inherited: the preconditioned Roe scheme [1], for instance, still suffers from shock-induced anomalies, such as the carbuncle phenomena in hypersonic flows. In addition, those schemes need at least one problem-dependent parameter, such as cutoff Mach number or freestream Mach number, which sometimes restricts the applicability of the scheme. This parameter should be a very small but nonzero number for very low Mach number flows, but the users inevitably encounter the problem of how to properly define such a number when no uniform flow is present (e.g., an internal flow). Thus, those schemes cannot be applied successfully for flows involving both low and high Mach number regions.

As another approach, an all-speed version of the Roe scheme was developed without relying on the cutoff Mach number in [4] but with additional parameters and reference values required instead. It will suffer from shock anomaly issues in a high Mach number regime as it recovers to the original Roe scheme.

On the other hand, a number of schemes have been proposed to overcome weaknesses of schemes in a high Mach number regime. Among them, the advection upstream splitting method (AUSM),

Presented as Paper 2009-0136 at the 47th AIAA Aerospace Sciences Meeting Including the New Horizons Forum and Aerospace Exposition, Orlando, FL, 5–8 January 2009; received 7 September 2010; revision received 28 February 2011; accepted for publication 10 March 2011.

*Senior Researcher and Director, JAXA's Engineering Digital Innovation Center, 3-1-1 Yoshinodai, Chuuou. Member AIAA.

†Researcher, JAXA's Engineering Digital Innovation Center, 3-1-1 Yoshinodai, Chuuou. Member AIAA.

originally developed by Liou and Steffen [5], and its variant AUSM-family schemes [6–8] are simple, yet accurate and robust, for high Mach number flows. Thus, they have been widely used as one of the standard methods of compressible CFD algorithms. In recent years, all-speed versions of AUSM-family schemes that can compute from very low Mach number to very high Mach number flows are also developed by Edwards [9] and Liou [10]. Schemes of this kind are very attractive for various applications, such as sound generation by supersonic plume, flows in a liquid rocket engine combustor, and cavitating gas–liquid flows. However, methods in [9,10] also include at least one problem-dependent parameter. In addition, the algorithm simplicity of the original AUSM was sacrificed in those methods.

Therefore, the purpose of this study is to develop an all-speed scheme of the AUSM-family that is in a simple form and free from reference parameters, such as cutoff Mach number. First, the AUSM-family schemes are briefly described, and then, a new simple flux function that reduces numerical dissipation in a low Mach number regime is introduced, which is named simple low-dissipation AUSM (SLAU) (Sec. II). By comparing with existing methods, advantages of the present scheme are demonstrated in applications to flow computations involving fundamental flow features, such as shock, vortex, boundary-layer separation, and sound propagations, in wide-ranging Mach number regimes (Sec. III). Finally, the concluding remarks will be given in Sec. IV.

II. New Numerical Flux for All Speeds

A. Basic Equation

Navier–Stokes equations (including the preconditioning matrix Γ, which is simply eliminated in the nonpreconditioned form) can be written in the finite volume form as

$$\frac{V_i}{\Delta t_i}\Delta \mathbf{Q}_i + \Gamma_i^{-1}\sum_j (\tilde{\mathbf{F}}_{i,j} - \tilde{\mathbf{R}}_{i,j}) s_{i,j} = 0 \tag{1a}$$

$$\mathbf{Q} = \begin{bmatrix} \rho \\ \rho u_l \\ e \end{bmatrix}, \qquad \mathbf{F}_k = \begin{bmatrix} \rho u_k \\ \rho u_l u_k + p\delta_{lk} \\ \rho u_k h \end{bmatrix}$$

$$\mathbf{R}_k = \begin{bmatrix} 0 \\ \tau_{lk} \\ u_m \tau_{mk} + (\kappa + \kappa_t)\frac{\partial T}{\partial x_k} \end{bmatrix} \tag{1b}$$

$$\tau_{lk} = (\mu + \mu_t)\left[\left(\frac{\partial u_l}{\partial x_k} + \frac{\partial u_k}{\partial x_l}\right) - \frac{2}{3}\frac{\partial u_n}{\partial x_n}\delta_{lk}\right] \tag{1c}$$

where $\tilde{\mathbf{F}}_{i,j}$ and $\tilde{\mathbf{R}}_{i,j}$ are inviscid and viscous fluxes, respectively; V_i, Δt_i, and $\Delta \mathbf{Q}_i$ are volume, time-step size, and change of conservative variables $\mathbf{Q}$, respectively, of cell i; and $s_{i,j}$ is the cell-interfacial area between cells i and j. As for flux vector components, ρ is the density, u_l are the velocity components in Cartesian coordinates, e is the total energy per unit volume, p is the pressure, h is the total enthalpy [$h = (e + p)/\rho$)], and T is the temperature. The working gas is air approximated by the calorically perfect gas model with the specific heat ratio $\gamma = 1.4$. The Prandtl number is $Pr = 0.72$. The molecular viscosity μ and thermal conductivity κ are related as $\kappa = c_p\mu/Pr$, where c_p is specific heat at constant pressure. In a turbulent case, the turbulent viscosity μ_t is given by a turbulence model and related as $\kappa_t = c_p\mu_t/Pr_t$, where Pr_t is the turbulent Prandtl number 0.89.

The inviscid flux computation is quite important in high Reynolds number flows, not to mention in inviscid flows. In this paper, only the inviscid flux term $\tilde{\mathbf{F}}_{i,j}$ is discussed, whereas the viscous term $\tilde{\mathbf{R}}_{i,j}$ is calculated according to Wang [11] in viscous cases, if not mentioned otherwise.

B. Brief Description of AUSM-Family Schemes

Numerical inviscid flux calculated by an AUSM-family scheme is generally expressed as follows: using extrapolated left-side (+) and right-side (−) cell-interface values of either first-order or higher-order via MUSCL,

$$\tilde{\mathbf{F}} = \frac{\dot{m} + |\dot{m}|}{2}\boldsymbol{\Phi}^+ + \frac{\dot{m} - |\dot{m}|}{2}\boldsymbol{\Phi}^- + \tilde{p}\mathbf{N} \tag{2}$$

$$\boldsymbol{\Phi} = (1, u, v, w, h)^T \tag{3}$$

$$\mathbf{N} = (0, x_n, y_n, z_n, 0)^T \tag{4}$$

$$h = (e + p)/\rho \tag{5}$$

Here, x_n, y_n, and z_n are Cartesian components of a normal vector from the left to the right; u, v, and w are velocities in the x, y, and z directions; and ρ, e, $\dot{m}$, and p represent density, total energy of unit volume, mass flux, and static pressure, respectively.

C. Correction on Pressure Flux for Low Dissipation at Low Dissipation at Low Mach Number

Most of the AUSM-family schemes use the following pressure term inherited from the flux vector splitting of van Leer [12]:

$$\tilde{p} = \beta^+ p^+ + \beta^- p^- \tag{6}$$

$$\beta^\pm = \begin{cases} \frac{1}{4}(2 \mp M^\pm)(M^\pm \pm 1)^2 \pm \alpha M^\pm (M^{\pm 2} - 1)^2, & |M^\pm| < 1 \\ \frac{1}{2}[1 + \mathrm{sign}(\pm M^\pm)], & \text{otherwise} \end{cases} \tag{7}$$

$$M^\pm = \frac{V_n^\pm}{\bar{c}} = \frac{u^\pm x_n + v^\pm y_n + w^\pm z_n}{\bar{c}} \tag{8}$$

We set $\alpha = 0$; that is, the higher-order term introduced by Liou [6] is eliminated in this study for brevity.

Equation (6) can be exactly rewritten as follows [9]:

$$\tilde{p} = \frac{p^+ + p^-}{2} + \frac{\beta^+ - \beta^-}{2}(p^+ - p^-) + (\beta^+ + \beta^- - 1)\frac{p^+ + p^-}{2} \tag{9}$$

The third term of Eq. (9) approaches the following notation in low Mach number limit by neglecting the higher terms of Mach number and by introducing the appropriate averaged sound speed,

$$(\beta^+ + \beta^- - 1)\frac{p^+ + p^-}{2} \Rightarrow \frac{3}{4\gamma}\frac{\rho^+ + \rho^-}{2}\bar{c}(V_n^+ - V_n^-) \tag{10}$$

We can see that this term works as numerical dissipation having a scale of sound speed. Thus, it is suitable for high subsonic speeds, whereas it is too large in low Mach number flows where the sound speed is orders larger than local fluid velocity [9]. (If we take the average sound speed as $\bar{c} = \sqrt{\gamma(p^+ + p^-)/(\rho^+ + \rho^-)}$, the preceding equation is exactly true; while it still holds approximately for another choice of $\bar{c}$, such as $\bar{c} = (c^+ + c^-)/2$. Thus, for simplicity, we employ $\bar{c} = (c^+ + c^-)/2$ in the rest of the present paper.) On the other hand, our preliminary numerical tests (although not shown here) showed that the simple averaged pressure [i.e., only the first term of Eq. (9), instead of full Eq. (9)] led to serious oscillations or divergence, even at low Mach number flows (where the second term is negligibly small); therefore, the dissipative effect of the pressure term [the third term of Eq. (9)] is essential for stability.

To control the magnitude of the dissipation while keeping stability, we replace the third term of Eq. (9) similarly to [9] but in a different way. We introduce the new form of the pressure term as

$$\tilde{p} = \frac{p^+ + p^-}{2} + \frac{\beta^+ - \beta^-}{2}(p^+ - p^-) + f_p \cdot (\beta^+ + \beta^- - 1)\frac{p^+ + p^-}{2} \tag{11}$$

Here, f_p is a nondimensional function to control numerical dissipation. For the third term to have the scale of convective velocity in a low Mach number regime while keeping the original form in higher Mach numbers, f_p should have the following features:

$$f_p \begin{cases} \propto |M| & |M| \ll 1 \\ =1 & |M| \geq 1 \end{cases} \tag{12}$$

As a simple and smooth function, the following form given by Eqs. (13–15) is chosen here:

$$f_p = 1 - \chi \tag{13}$$

$$\chi = (1 - \widehat{M})^2 \tag{14}$$

$$\widehat{M} = \min\left(1.0, \frac{1}{\bar{c}}\sqrt{\frac{u^{+2} + v^{+2} + w^{+2} + u^{-2} + v^{-2} + w^{-2}}{2}}\right) \tag{15}$$

where f_p is similar to f_a in AUSM$^+$-up[‡] [10] [Eq. (16)] and simpler than $f(M)$ in [4] or others [1,9]. This function shows an asymptotic behavior against the local Mach number, as shown in Fig. 1. One may note that f_p in the present method and f_a in [10] showed the same trend (for $M > M_\infty$), because the formulations look mathematically the same to each other; however, in actual implementation, f_a in [10] is cut off at the prescribed value of M_∞, whereas f_p in the present scheme asymptotes to zero as the local Mach number. Furthermore, they are based on totally different definitions for the local Mach numbers: AUSM$^+$-up [10] employed only the normal component but with freestream Mach number M_∞, as shown in Eq. (17), whereas the present scheme in Eq. (13) uses multidimensional velocity and no reference value. The role of the multidimensional velocity will be demonstrated later in Sec. III.K:

$$f_a(M_O) = M_O(2 - M_O)\text{: scaling function in AUSM}^+\text{-up} \tag{16}$$

$$M_O^2 = \min[1.0, \max(\bar{M}^2, M_\infty^2)], \quad \bar{M}^2 = (V_n^{+2} + V_n^{-2})/2a_{1/2}^2 \tag{17}$$

In addition, the present modification in Eqs. (11–15) does not violate the contact discontinuity-preserving nature of most of the AUSM-family schemes. For example, assuming $p^+ = p^-$ and all the velocity components are zero ($\beta^+ = \beta^- = 0$), the pressure flux in Eq. (11) merely gives $\tilde{p} = p^+ = p^-$, as it should be.

The pressure term was also modified in other all-speed AUSM schemes [9,10] but in elaborate manners with problem-dependent parameters involved. Our method presented herein is free from these restrictions; thus, its extensive applicability is expected.

Note that the present modification is active only in low Mach number regimes, and the original scheme is recovered otherwise. Thus, the pressure term of the form of Eq. (11) will be used for the rest of the paper.

Careful readers may wonder if the interface pressure given by Eq. (11) still holds for incompressible flow limit where variables absent from incompressible flow expression, such as absolute pressure or speed of sound, play roles. If we split pressure into its reference value and variation as $p = p_{\text{ref}} + p'$, we can rewrite the interface pressure of Eq. (11) as

$$\tilde{p}' = \frac{p'^+ + p'^-}{2} + \frac{\beta^+ - \beta^-}{2}(p'^+ - p'^-) + f_p \cdot (\beta^+ + \beta^- - 1)\left[\frac{p'^+ + p'^-}{2} + p_{\text{ref}}\right]$$

[‡]See Appendices A and B for full descriptions of SLAU and AUSM$^+$-up, respectively.

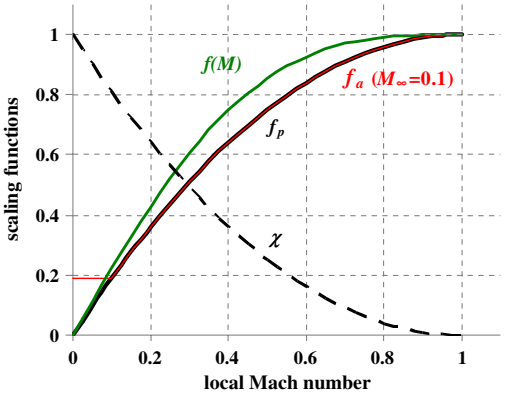

Fig. 1 Mach number effects of χ and other scaling functions.

Then, we realize that the reference pressure remains in the last parentheses of the last term. With incompressible limit $M \to 0$ [as in Eq. (10)], however, the last term $f_p \cdot (\beta^+ + \beta^- - 1)p_{\text{ref}}$ leads to

$$\frac{3}{2\gamma}\rho_{\text{ref}}\sqrt{\frac{u^{+2} + v^{+2} + w^{+2} + u^{-2} + v^{-2} + w^{-2}}{2}}(V_n^+ - V_n^-)$$

by using f_p defined by Eqs. (10–15). Thus, this form is totally free from the reference pressure or the speed of sound; hence, it is suitable for incompressible flow as long as an ideal gas is assumed and the present notation is valid (extensions to real fluids are left as a future work). Also note that we can use p' instead of p for reconstructing the primitive variable in the MUSCL approach.

D. Selection of Mass Flux

It is known that various functions can be used as the mass flux function of AUSM-type schemes. Among many methods, the mass flux of Courant–Isaacson–Rees schemes for the locally linearized Euler equation, which is rather well known as the Roe scheme, written in primitive variables is used as a starting point in this section for the following reasons:

1) It is exact in the sense of the upwind scheme for a locally linearized Euler equation.

2) The role of each term can be clearly seen, as will be stated.

3) The resultant schemes using this mass flux suppress the overshoot if a first-order scheme or a higher-order scheme with a proper slope limiter is used, whereas original AUSM is known to produce overshoot at shock front, even in a first-order scheme.

The mass flux function is written as

$$\dot{m} = \frac{1}{2}\{(\rho V_n)^+ + (\rho V_n)^-\} - \frac{1}{2}|\bar{V}_n|\Delta\rho - \frac{|\bar{M}+1| - |\bar{M}-1|}{4}\bar{\rho}\Delta V_n - \frac{|\bar{M}+1| + |\bar{M}-1| - 2|\bar{M}|}{4\bar{c}}\Delta p \tag{18}$$

$$\Delta q = q^- - q^+ \tag{19}$$

where $(\bar{\ })$ stands for arithmetic averages of both sides (Roe averaging is not used).

Each term of the mass flux can be interpreted as follows:

1) The first term denotes the average of the left and right states.

2) The second term is named as the density difference term and denotes the direct diffusion term.

3) The third term is denoted as the velocity difference term.

4) The fourth term is denoted as the pressure difference term, or simply the pressure term, representing acoustic damping, because the term can be rewritten under isentropic conditions as

$$\frac{|\bar{M}+1| + |\bar{M}-1| - 2|\bar{M}|}{2\bar{c}}\Delta p \approx \frac{|\bar{M}+1| + |\bar{M}-1| - 2|\bar{M}|}{2}\bar{c}\Delta\rho \tag{20}$$

$$\because \Delta p \approx \bar{c}^2 \Delta\rho \tag{21}$$

The scheme using this mass flux was named the simple high-resolution upwind scheme (SHUS) [8] (or denoted as AUSM$^+$-R in [13]), and its low-dissipation version, which used pressure flux in Eq. (11), was named low-dissipation SHUS [14]. Although these schemes are more robust than the Roe scheme, they still encountered the carbuncle phenomena (i.e., a multidimensional mode of shock instabilities [15]) in a shock propagation problem in a two-dimensional channel [16]. According to Liou [13], a mass flux that contains a pressure difference term tends to exhibit the carbuncle (shown later in Sec. III.B). Thus, this drawback had been expected to be cured by elimination of the pressure difference term (Δp term, the last term) in Eq. (18). However, from our preliminary investigation, this modification turned out to be a failure. The modified flux, in a genuine one-dimensional (1-D) setup, showed the overshoot at a shock front again. It is due to cancellation of the dissipation effects of the second term ($\Delta\rho$ term) by the third term (ΔV_n term), considering the fact that these terms have opposite signs across the shock where the flow is compressed ($\Delta\rho > 0$) and decelerated ($\Delta V_n < 0$). In other words, the original form of Eq. (18) appeared to have created a proper amount of dissipation in a direction normal to the shock (1-D stable) but not in its parallel direction (multidimensional unstable); whereas the modified form (no Δp term) is appropriate only for suppression of the shock instability in its parallel direction (multidimensional stable) but suffers from 1-D anomaly (1-D oscillation). This discussion is summarized in Table 1, consistent with the results for other schemes [15]. Thus, as suggested by Kitamura et al. [15], the dissipation additions in the shock normal and parallel directions should be considered separately, so that the parallel component is less dissipative than the normal one in the designing of a universally stable scheme.

Table 1 Relation between dissipation addition to the present Euler flux with shock anomalies

Shock anomalies	1-D (normal to shock)	Multidimensional (parallel to shock)
Equation (18) (original)	Stable	Unstable/oscillatory
Equation (18) without Δp term (less dissipative)	Oscillatory	Stable

The other existing mass flux functions can be decomposed into the similar terms. For example, the mass flux of the original AUSM has a form of a combination of 1–3, stated previously (i.e., without the pressure difference term). In other words, practically usable fluxes can be developed without the pressure difference term. Thus, it is assumed that all the terms of Eq. (18) are not always necessary for the formulation of mass flux schemes. To see the effect of each term more clearly, we consider the simplest mass flux formula here.

The combination of the 1) average term and 2) the density difference term forms a very simple scheme:

$$\dot{m} = \tfrac{1}{2}\{(\rho V_n)^+ + (\rho V_n)^- - |\bar{V}_n|\Delta\rho\} \tag{22}$$

$$|\bar{V}_n| = \frac{\rho^+|V_n^+| + \rho^-|V_n^-|}{\rho^+ + \rho^-} \tag{23}$$

The mean normal velocity $|\bar{V}_n|$ in Eq. (22) can arbitrarily be chosen. However, it was reported that the simple average $0.5(|V_n^+| + |V_n^-|)$ had unphysically prevented a supersonic jet of a light gas from coming into the computational domain filled with a heavy gas at the inlet boundary.[§] For instance, even when a positive inflow condition, $\rho^+ = 1$, $V_n^+ = 4$, $\rho^- = 7$, $V_n^- = 0$, is prescribed at the inlet boundary, Eq. (22) leads to negative ($\dot{m} = -4 < 0$) for $|\bar{V}_n| = 0.5(|V_n^+| + |V_n^-|) = 2$, whereas the positive incoming flow is realized ($\dot{m} = 0.5 > 0$) for the choice of Eq. (23), $|\bar{V}_n| = 0.5$. Thus, the present form in Eq. (23) is used in this study. Equation (22) can be rewritten as follows, and it is clearly seen that the resultant mass flux will have a positive/negative sign if velocities at both sides are positive/negative:

$$\dot{m} = \frac{\rho^+\{\rho^+(V_n^+ + |V_n^+|) + \rho^-(V_n^+ - |V_n^+|)\} + \rho^-\{\rho^+(V_n^- + |V_n^-|) + \rho^-(V_n^- - |V_n^-|)\}}{2(\rho^+ + \rho^-)} \tag{24a}$$

$$\dot{m} = \rho^+(V_n^+ + V_n^-) > 0 \quad \text{if } V_n^+, V_n^- > 0 \tag{24b}$$

$$\dot{m} = \rho^-(V_n^+ + V_n^-) < 0 \quad \text{if } V_n^+, V_n^- < 0 \tag{24c}$$

Obviously, a simpler and symmetric mass flux than the preceding is merely the central difference scheme, but it is known that this scheme will not give sufficient solutions for discontinuities. Therefore, Eq. (22) seems to be the simplest mass flux functions for AUSM-type schemes. Surprisingly, this simple scheme turned out to be practically usable enough for over subsonic speed according to our experience, but this scheme itself will not be discussed further in the rest of the paper; instead, we consider introduction of an additional term to Eq. (22).

Note again that this function still gives correct mass flux, i.e., no flux for a stationary or a moving contact discontinuity where pressure and (normal) velocity are constant on both sides.

This version will be further improved in the following subsection.

E. Corrections on Mass Flux for High and Low Mach Numbers

In our experience, the scheme in Eqs. (22) and (23) is acceptable for moderate flow conditions, such as a transonic flow past an airfoil. However, in extreme situations, such as a flow with an asymmetric strong expansion, the following remedy should be introduced; otherwise, the flux results in a negative internal energy at the interface:

$$\dot{m} = \tfrac{1}{2}\{(\rho V_n)^+ + (\rho V_n)^- - |\bar{V}_n|\Delta\rho\} f_\rho \tag{25}$$

To give a proper mass flux for the supersonic expansion case, we require the following features for f_ρ as

$$f_\rho = \begin{cases} \approx 1 & \text{nonexpansion case} \\ = 0 & \text{supersonic strong expansion case} \end{cases} \tag{26}$$

As a simple continuous function that satisfies the preceding requirement, the following form is selected:

$$f_\rho = 1 - g \tag{27}$$

$$\left.\begin{aligned} g &= g^+ \cdot g^- \in [0, 1]; \\ g^+ &= -\max[\min(M^+, 0), -1], \quad g^- = \min[\max(M^-, 0), 1] \end{aligned}\right\} \tag{28}$$

where M^+ and M^- are Mach numbers normal to the cell interface defined in Eq. (8).

The behaviors of g^+ and g^- are shown in Fig. 2: the function $g = g^+ g^-$ works at a strong expansion ($M^+ < -1$ and $M^- > 1$); then, $f_\rho = 0$ ($g = 1$) and Eq. (25) produces no (unphysical) flux.

[§]Private communication with Seiji Tsutsumi, Japan Aerospace Exploration Agency, October 2008.

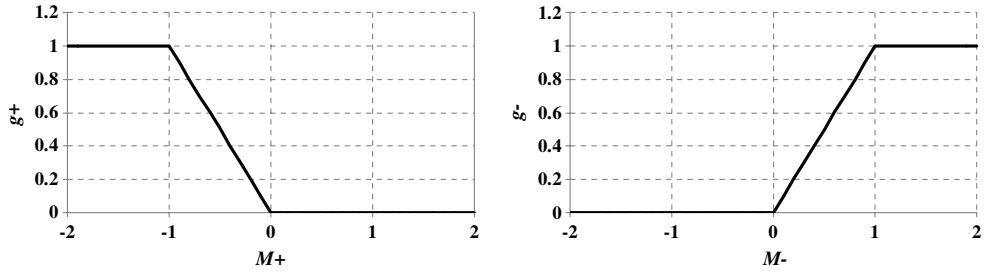

Fig. 2 Mach number effects of a) g^+ and b) g^-.

Thus, the way of elimination of unphysical flux at expansion cases in SLAU is different from that in the exact Riemann flux. One may find it ad hoc to introduce the function g, but we stress here that g is activated only when it is needed; otherwise, Eq. (25) recovers to Eq. (22), which expresses physics in a simple manner. In other words, g is designed as simple a function as possible, which eliminates unphysical solutions at a strong expansion yet avoids deviations from the original formulation. Its effect will be demonstrated in Sec. III. Furthermore, numerical tests (to be shown) demonstrate that at subsonic speeds, $g(0 < g < 1)$ does not harm the solutions at all (any more complex treatments actually gave no practical improvements in our experience). From all those reasons, the form of Eq. (25) is adopted here.

Here, we consider the Δp term again. Although Eq. (25) gave satisfactory solutions for over high subsonic flows, it produced numerical oscillations in low Mach numbers (Fig. 3a), whereas Eq. (18) did not (not shown). This means that the Δp term in Eq. (18) has a favorable effect in stabilizing low-speed flow computations. Thus, we consider recovering the term that was once eliminated from Eq. (18) but used only in a low Mach number regime.

The Δp term in Eq. (18) was designed to be active only in subsonic flows; however, Table 1 shows that the term plays a role in even high-speed flows in the direction normal to the shock wave. This favorable effect works in the subsonic portion of a numerically captured shock structure; on the other hand, the term behaves in an undesired manner in the parallel direction to the shock, where propagation of numerical disturbance is encouraged inside the shock. Thus, the dissipation produced by the pressure difference term should be alleviated in the shock-parallel direction for high-speed flow computations. Considering these, the Δp term, which is fully active only in very low Mach numbers and partly active at the shock, is introduced to Eq. (25) as follows:

$$\dot{m} = \frac{1}{2}\{(\rho V_n)^+ + (\rho V_n)^- - |\bar{V}_n|\Delta\rho\}(1-g) - \frac{\chi}{2\bar{c}}\Delta p \qquad (29)$$

The scheme is smoothly switched from the low-speed mode to the high-speed one, while its simplicity is maintained by employing the common function χ in Eqs. (14) and (15). The flux function using this mass flux function is SLAU. Figure 3b clearly shows SLAU suppressed instability arose in Fig. 3a. One of the major differences between the pressure terms (in the mass fluxes) of Eq. (18) and SLAU is in its behavior in the crossflow direction. The pressure function of Eq. (18) (the last term) is turned off only in the stream direction in the high Mach number region. On the other hand, the pressure function of SLAU [Eq. (29)] is designed to be turned off in all the directions for high Mach flows.

Now, the new numerical flux scheme named SLAU is derived by combining the mass flux function in Eq. (29) with Eq. (23) and the pressure function of Eqs. (11–15). The final form of the proposed scheme appears also in Appendix A. Its performance will be demonstrated in the next section. The key features of SLAU are summarized as follows:

1) The pressure term was modified to achieve a low-dissipation property in a very low Mach number regime. This modification employed multidimensional velocity components and no problem-dependent parameters (e.g., cutoff Mach number) in contrast with [9,10]; hence, its extensive applicability is expected.

2) Unphysical solutions at low and hypersonic speeds are avoided by introduction of simple functions χ and g, which are active only when needed.

3) In spite of those modifications, the present scheme is parameter free and simpler than the existing all-speed schemes [9,10].

III. Numerical Examples

A series of test cases are presented in the following.

First, high Mach number cases will show the robustness of SLAU against known pathological behaviors appearing in some methods and/or conditions. Then, test cases for low speeds (including aero-acoustic simulations) will be presented to demonstrate that SLAU

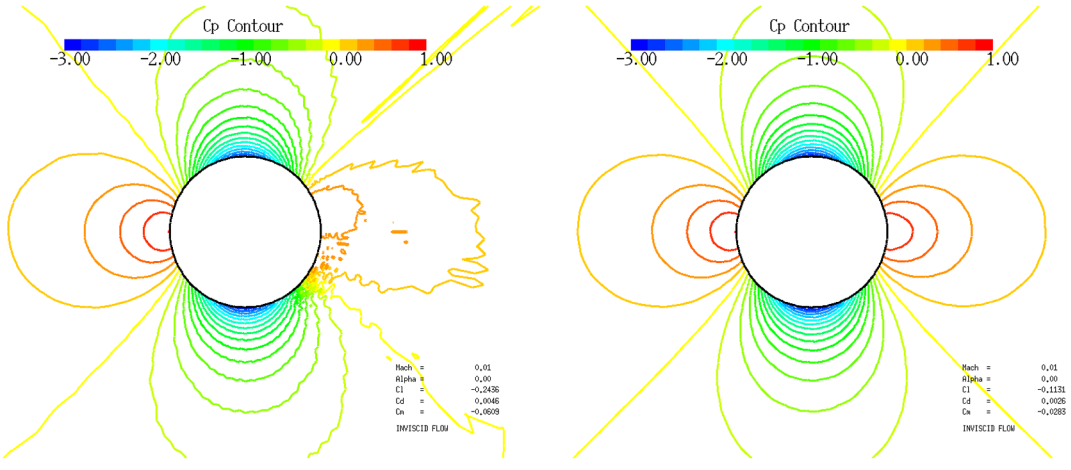

Fig. 3 Pressure contours for $M = 0.01$ circular cylinder flow computed by SLAU a) without Δp term [Eq. (25)] and b) with Δp term [Eq. (29)].

can deal with low-speed flows with desirable accuracy and robustness. (As for further comparisons with existing all-speed methods, see [17], in which performances of SLAU are compared in detail with those of other all-speed schemes in several numerical tests at low speeds.) Finally, moderate Mach number cases will be conducted to primarily demonstrate that the typical solutions are obtained by SLAU with and without viscous effects.

SLAU is compared with two well-known numerical fluxes: AUSM+ [6] and Roe [18] (with entropy fix, for hypersonic cases). AUSM+ is one of predecessors of SLAU, and it known as one of the robust schemes against shock anomalies. The Roe flux is the approximate Riemann solver and known to be vulnerable to carbuncle phenomena.

The default numerical schemes and setups are described in the following: a cell-centered finite volume formulation along with the third-order MUSCL approach is used for spatial discretization; an lower–upper symmetric Gauss–Seidel (LU-SGS)-type implicit time integration in these computations [19,20]; and the boundary conditions are given by controlling values in the ghost cells. The far-field boundary condition is given by freezing the values in ghost cells to the far-field values. Although values in ghost cells are not changed, flux at the interfaces varies reflecting internal values by the approximate upwind nature of the numerical fluxes. Thus, this treatment is regarded as an approximate characteristic boundary condition. For the solid wall, the density and pressure of ghost cells are given by zeroth-order extrapolation. Point symmetric or mirror symmetric velocity vectors are set for nonslip and slip walls, respectively.

A. Hypersonic Flow Around Two-Dimensional Blunt Body (High Mach Number)

We solved the Euler equations and computed a two-dimensional blunt-body flow at $M_\infty = 8.1$. The computational grid consists of 160(circumferential) × 80(wall normal) cells without any stretching, clustering, or shock alignment (Figs. 4a and 4b). The inflow (freestream) boundary is 1.5 times the radius away from the wall. The slip condition is used at the wall, and the other two are outflow boundaries where the internal variables are merely extrapolated.

The first-order schemes, both in time (forward Euler) and space, are used with Courant–Friedrichs–Lewy (CFL) = 0.5. All the cases reached machine-zero convergence at around 30,000 steps or earlier, and the results are shown in Figs. 4c–4e. The present scheme (Fig. 4c), similar to AUSM+ (Fig. 4d), is free from shock anomalies, such as carbuncle phenomena in Roe (E-Fix: Harten's entropy fix) (Fig. 4e). Furthermore, the captured shock is very smooth but rather thicker in SLAU compared with AUSM+, which is affected by the relative position to the grid line [15]. In spite of this, the broader shock captured by SLAU does not degrade the solution at all. This is demonstrated in Fig. 5, in which the pressure and temperature profiles along the centerline (x: its origin corresponds to the

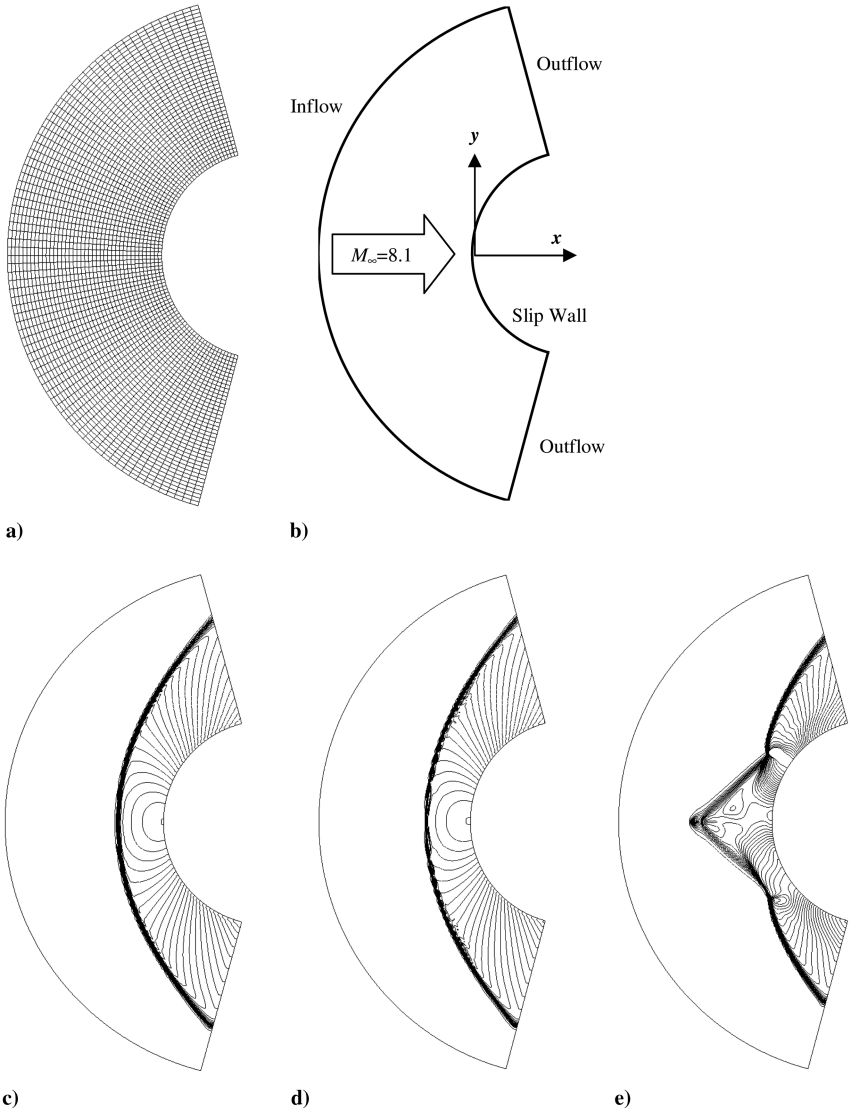

Fig. 4 Grid coordinates and results (32 contour lines for $1.5 < P/P_\infty < 84.0$) for $M\infty = 8.1$ blunt-body test: a) grid (160 × 80 cells; every other line displayed), b) coordinates, c) SLAU, d) AUSM+, and e) Roe (E-Fix).

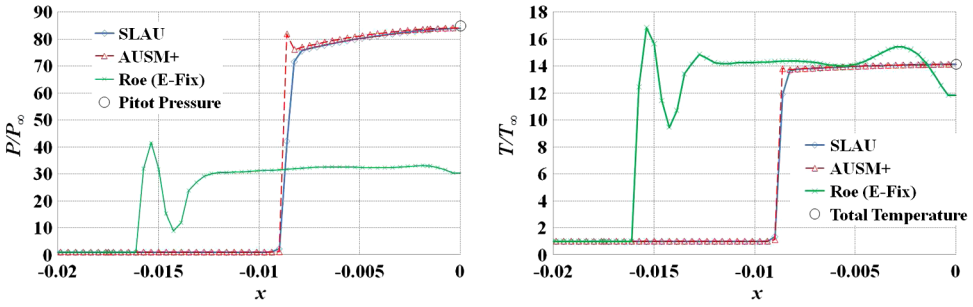

Fig. 5 Profiles along centerline: a) pressure and b) temperature.

stagnation point) are extracted from each case, as well as stagnation values shown in Table 2; SLAU gave correct behavior of pressure/temperature jump at the shock, and stagnation values showed around 1% error from pitot pressure, $P_0/P_\infty = 84.94$ and excellent agreement with total temperature, $T_0/T_\infty = 14.12$. AUSM+, as well as SLAU, has a total enthalpy-preserving property, and the stagnation temperature was well predicted, but its pressure profile showed a small overshoot at the shock (Fig. 5a); Roe (E-Fix) showed poor profiles (Figs. 5a and 5b) due to the carbuncle.

Therefore, a satisfactory solution that is not perturbed by the grid geometry (as in the next example) has been obtained by SLAU in this case (although Kitamura et al. pointed out in [15,21] that any flux functions can suffer from shock anomalies under certain setups). SLAU has been shown to be slightly more diffusive than AUSM+ at a high Mach number (Figs. 4c and 4d), but it has enough resolution of shocks and boundary layers and shows low dissipation at low Mach numbers (as will be shown). These issues will appear in the following numerical examples.

B. One-Dimensional Shock Propagation in Two-Dimensional Channel (High Mach Number, Unsteady)

As pointed out by Quirk [16], 1-D shock propagations computed using a distorted two-dimensional mesh sometimes show instabilities. The same test is conducted here, and first-order schemes both in time (forward Euler) and space are used. A Mach 6 normal shock propagation from left to right is computed in a uniformly spaced two-dimensional domain having 20×800 (flow direction) cells (each cell width is 0.05) with $\pm 1.e-6$ perturbations at the centerline of the channel. Euler equations are solved with CFL = 0.461. Upper and lower boundaries are treated as slip walls, inflow and outflow conditions are fixed to initial conditions on both sides of the shock front, and the whole domain is filled with a stationary gas at the initial stage. The computation is terminated before the shock reaches the outflow boundary. Detailed information on computational grids and conditions can be found in [16]. The results at 1000 time steps are shown in Fig. 6. It is known that the Roe scheme exhibits the instabilities, and SHUS, presented in Eq. (18) as a predecessor of SLAU, also did (Fig. 6b). On the other hand, SLAU did not suffer from such instabilities (Fig. 6a).

C. Double Mach Reflection (High Mach Numbers, Unsteady)

A planar shock wave propagating in inviscid fluid at Mach 10 reflected by a 30 deg ramp was computed using several numerical flux functions and compared. A second-order-accurate two-step explicit scheme was used for time integration with courant number 0.52, and a second-order spatial accuracy was achieved by reconstruction of primitive variables with van Albada's limiter [22]. The grid used has 300×1200 cells. The lower boundary is treated as slip wall, and the left and the right boundary values are fixed to the left and right states of the shock wave. The condition on the upper boundary is temporally changed according to the shock propagation.

Table 2 Computed stagnation pressure/temperature

Flux function	SLAU	AUSM+	Roe (E-Fix)	Theoretical values
P_0/P_∞	84.02	84.05	30.36	84.94
T_0/T_∞	14.12	14.13	11.84	14.12

The jet remains between the legs of the bifurcation shock in solutions by AUSM+ and SLAU (Figs. 7a and 7b), whereas the result by the Roe scheme shows that a jet blowing rightward along the wall interacts with the shock (Fig. 7c). In such a complex flowfield, it is generally difficult to distinguish the shock anomalies like carbuncle phenomena from physical complex shock structures. However, considering characteristics of the Roe scheme for the normal shock seen in the preceding subsections, it appears reasonable to say that the solution in the Roe case is contaminated by the carbuncle phenomena and that SLAU, as well as AUSM+, reproduced a physical solution. This example clearly highlighted the importance of suppressing the carbuncle phenomena by the numerical method; otherwise, the computed flowfields are misunderstood and the reliability of the numerical solution will be degraded considerably.

D. Removal of Expansion Shock (High Mach Number, Unsteady)

In this set of cases, the Rankine–Hugoniot relation for a $M_\infty = 3$ inviscid flow is imposed across the initial discontinuity where velocity directions are flipped over [23] for left (L: $i \le 25$) and right (R: $i \ge 26$) states:

$$\mathbf{Q}_L = \begin{bmatrix} f(M_\infty) \\ 1 \\ 0 \\ \frac{g(M_\infty)}{\gamma(\gamma-1)M_\infty^2} + \frac{1}{2f(M_\infty)} \end{bmatrix}, \qquad \mathbf{Q}_R = \begin{bmatrix} 1 \\ 1 \\ 0 \\ \frac{1}{\gamma(\gamma-1)M_\infty^2} + \frac{1}{2} \end{bmatrix} \tag{30a}$$

where

$$f(M_\infty) = \left(\frac{2}{(\gamma+1)M_\infty^2} + \frac{\gamma-1}{\gamma+1} \right)^{-1}$$
$$g(M_\infty) = \frac{2\gamma M_\infty^2}{\gamma+1} - \frac{\gamma-1}{\gamma+1} \tag{30b}$$

The computational domain has 50 cells evenly spaced in one dimension. The left and right boundary conditions are inflow and outflow, respectively, where zero slopes are prescribed. Computations were conducted with the first order in both space and time (forward Euler) with CFL = 0.65. Only the results of $M_\infty = 3$ at 10 time steps are shown in Fig. 8. As is well known, Roe (without E-fix) produced an expansion shock, and AUSM+ suffered from this problem, as reported in [10]. On the other hand, SLAU successfully eliminated such an unphysical discontinuity, showing a smooth transition from subsonic to supersonic states. We also point out that this behavior is realized even when g is turned off [the result of SLAU ($g = 0$) was indistinguishable from the SLAU result, thus omitted in Fig. 8].

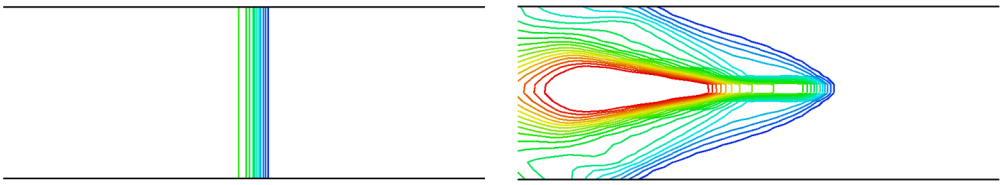

a) b)

Fig. 6 Density contours of propagating shock in two-dimensional channel using distorted mesh [16]. Results of a) SLAU and b) SHUS at 1000 steps are shown.

E. Symmetric and Asymmetric Supersonic Expansions (High Mach Numbers, Unsteady)

To see the effect of function g in the present scheme, we solve 1-D expansion problems with the following two initial conditions: 1) $M_L = -10$, $\rho_L = 1$, $M_R = 10$, $\rho_R = 1$, and $\rho_L u_L = \rho_R u_R = 1$; and 2) $M_L = -10$, $\rho_L = 1$, $M_R = 20$, $\rho_R = 1$, and $\rho_L u_L = \rho_R u_R = 1$, for left ($L$: $i \leq 25$) and right (R: $i \geq 26$). The results are shown in Fig. 9. These results clearly show that SLAU, as well as AUSM+, gives a physical solution for the asymmetric supersonic expansion thanks to g, whereas there is no role played by g for the symmetric case. On the other hand, the computation using the Roe scheme diverged.

F. D'Alembert's Paradox (Low and Moderate Mach Numbers)

In this example, we compute an inviscid flow around a circular cylinder. It is known as D'Alembert's paradox, in which the two-dimensional object in inviscid subsonic flow has no aerodynamic drag; however, in computations, the drag is actually introduced in the form of the numerical errors. In this computation, the surface of the cylinder is treated as the slip wall and the outer boundary condition is fixed to that of uniform flow. Polar mesh is used, and the cell number is 200 (azimuthal) × 50 (radial). The outer boundary is located at $100R$ (R: radius), and the smallest mesh size at the cylinder surface is $0.01R$. The mesh stretching ratio is about 1.16. The computed drag coefficients of a circular cylinder in inviscid flows of several Mach numbers are compared in Fig. 10 (the computed flowfield for SLAU was already shown in Fig. 3b). Excessive numerical dissipation in the Roe scheme or AUSM+ generated huge and divergent errors in very low Mach numbers. On the other hand, SLAU showed a much smaller error, which is almost independent on the Mach number. The absolute level of drag as an indicator of numerical error will be different if the grid is different. Thus, it is worth comparing only relative differences due to the numerical flux scheme.

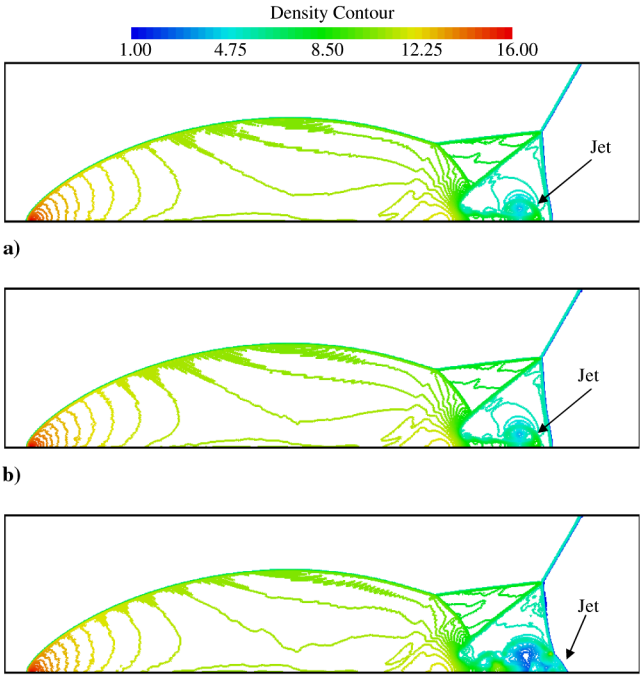

a) b) c)

Fig. 7 Double Mach reflection computed using a) SLAU, b) AUSM+, and c) Roe. Carbuncle phenomena are seen in result of Roe scheme.

G. Convergence Acceleration by Combination with Time-Derivative Preconditioning (Low Mach Number)

SLAU does not use the scaling of numerical viscosity derived from the preconditioning matrix; thus, it can be used without the preconditioning matrix. Nevertheless, the effectiveness of the combination with preconditioning on the time derivative is examined for a low Mach number flow ($M_\infty = 0.001$ around a cylinder). The mesh and boundary condition used is the same as the previous subsection. It is shown in Fig. 11 that the drag coefficient converged in a few 100 steps with the time-derivative preconditioning method of Weiss and Smith, as in [1,3], whereas it did not converge until several 10,000 steps without the preconditioning. Thus, SLAU can compute very low Mach number flows efficiently with the time-derivative preconditioning.

H. Stationary Rankine Vortex (Low Mach Number, Unsteady)

Preservation of vortices is crucial for accurate computations of unsteady separated flows. This nature is largely affected by the amount of the numerical dissipation. To investigate this property of the SLAU scheme, a stationary Rankine vortex is computed by several methods, where its radius is twice as large as the grid size ($R = 2\Delta x$, Δx: cell width) and the peak Mach number is set to 0.01. Regular structured mesh (cell) of 100×100(=50 R × 50 R, R: radius) is used at the center region, and stretched mesh is used in the outer region. The total mesh size is 300×300. The size of the whole computational domain is $1050R \times 1050R$. The whole outer boundary is fixed to a steady condition. The two-stage explicit Runge–Kutta scheme was used for the time integration. As shown in Figs. 12 and 13, the computed vortex by the Roe scheme or AUSM+ was smeared out, while that of SLAU almost kept the initial shape of the vortex.

I. Separated Flows Around a Circular Cylinder (Low Mach Number, Viscous, Unsteady)

As a typical low Mach number unsteady flow, separated flow around a circular cylinder is computed. Polar-type grids of several mesh densities are used. For the time integration, a three-point

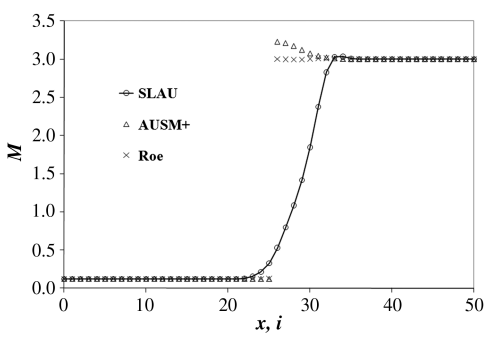

Fig. 8 Removal of expansion shock.

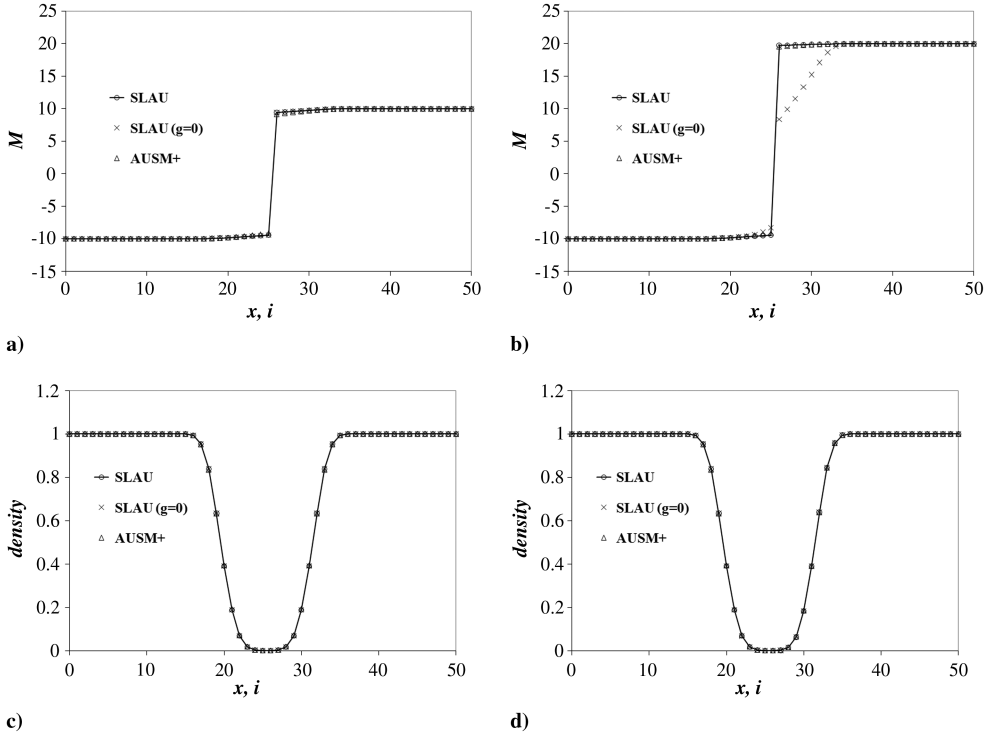

Fig. 9 Supersonic expansion results: a) symmetric (Mach number), b) asymmetric (Mach number), c) symmetric (density), and d) asymmetric (density).

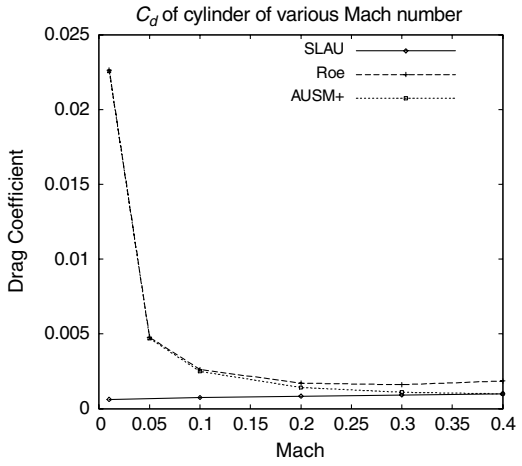

Fig. 10 Mach number dependency on aerodynamic drag of cylinder in inviscid flow.

backward Euler scheme using a matrix free Gauss–Seidel (MFGS; see Appendix E) implicit algorithm (one of the LU-SGS-type schemes) [20] is employed with nonlinear inner iterations.

Two Reynolds number cases are computed. The first one is the low Reynolds number case with $Re = 100$ (and $M = 0.01$), in which periodic shedding of Karman vortices ($St \approx 0.16$ [24]) should be observed. The radius of the computational domain is 200 times the cylinder radius R, and the smallest mesh size in radial direction is $0.01R$. The mesh sizes and stretching ratio are shown in Table 3. The velocity contours using the coarse mesh computed by SLAU and Roe schemes are shown in Fig. 14. Periodic vortex shedding is found in the result of SLAU; on the other hand, the Roe scheme produces steady separated flow. In the Roe case, huge numerical dissipation, which is produced by usual numerical flux functions, appeared to have suppressed the growth of instability. Time histories of the lift coefficients of each case are shown in Fig. 15. It is seen that, if we use the medium mesh, even the Roe scheme reproduces vortex shedding, yet the growth of oscillation is slower than that in SLAU. On the other hand, SLAU with medium mesh gives the almost identical history with the fine mesh case, showing that the mesh convergence is

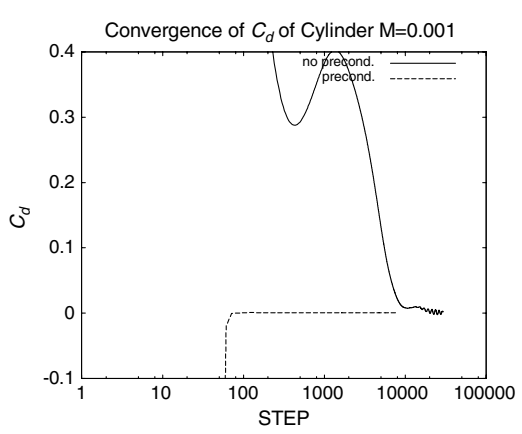

Fig. 11 Convergence histories of computed drag coefficient of a cylinder in inviscid flow at $M_\infty = 0.001$.

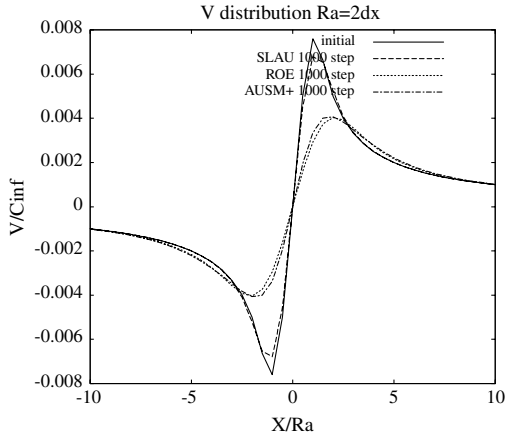

Fig. 12 Velocity profiles of a Rankine vortex after 1000 steps computed by several methods.

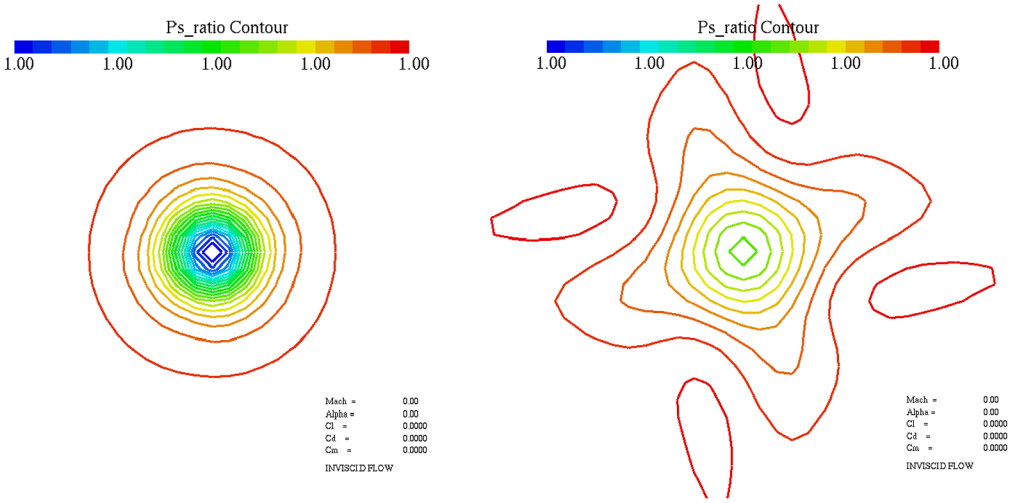

a) b)

Fig. 13 Pressure contours of stationary Rankine vortex computed using a) SLAU and b) Roe.

achieved with the medium mesh size. In Table 3, Strouhal numbers of vortex shedding are compared. Again, it is shown that SLAU with the coarse mesh is more accurate than the Roe scheme with medium mesh.

The second case is the high Reynolds number case with $Re = 10^5$, in which random shedding of small vortices should be observed. For this case, the size of the mesh is 200×200, the radius of the computational domain is $100R$, and the minimum mesh size is set to $10^{-4}R$. Pressure contours by the SLAU and Roe schemes are shown in Fig. 16. It is found that many small vortices are shed in the result of SLAU, whereas they are all smeared out in that of the Roe scheme.

J. One-Dimensional Sound Propagation (Low Mach Number, Unsteady)

As the present scheme is based on unpreconditioned compressible flow equations, it is naturally expected that it can compute sound propagations directly. Figure 17 compares the computed results of 1-D sound propagations using SLAU and Roe. Again, the two-stage explicit Runge–Kutta scheme is used for the time integration, the courant number is 0.5, and the wavelength l is set to $20\Delta x$ here (Δx: cell width). The cells are uniform up to $x = 2.0$ ($=20l$), and highly stretched meshes are used outside to damp the sound propagation in order to mimic the nonreflecting boundary. The inflow condition is given by setting the value in the ghost cell to the prescribed isentropic acoustic wave, and the outflow is fixed to the steady gas. According to the results, Roe showed faster decay of acoustic wave amplitude than SLAU; in other words, SLAU exhibited lower dissipation than the Roe scheme.

Then, the wavelength-to-cell-width ratio ($l/\Delta x$) is varied, and its effect on the decay of the wave is examined. Here, the decay ratio ε is defined:

$$A = A_0(1 - \varepsilon)^{x/l} \tag{31}$$

where A is the wave amplitude, and A_0 is the amplitude at $x = 0$. With A and A_0, the amplitudes of the pressure fluctuations are approximated.

Figure 18 compares the decay ratio ε of the SLAU and Roe schemes for one wavelength propagation with different ($l/\Delta x$). It is shown that the decay ratio ε reduces with larger ($l/\Delta x$) (i.e., higher numbers of grid points per wavelength) and that ε for SLAU is about a half of that for the Roe scheme for any ($l/\Delta x$). Therefore, it is demonstrated that SLAU can be applied for aeroacoustic simulations with better accuracy than the Roe scheme.

K. Euler Solution of NACA0012 Airfoil (Moderate Mach Numbers)

Computed pressure profiles on a NACA0012 airfoil at a 3° angle of attack of several Mach numbers ($M_\infty = 0.1$, 0.6, and 0.7) are shown in Fig. 19. The surface of the airfoil is treated as the slip wall, and the outer boundary condition is fixed to that of uniform flow. An O-type mesh is used, and the cell number is 400(circumferential)× 70(wall normal). The outer boundary is located at $100C$ (C: chord length), and the smallest mesh size on the airfoil surface is $10^{-4}C$. Thus, the mesh stretching ratio is about 1.190. The Roe scheme and SLAU are used with second-order MUSCL along with van Albada's limiter [22]. This example is selected to demonstrate that both results are almost identical and show no oscillations, regardless of the choice of Mach numbers.

In addition, we intentionally eliminated multidimensional components in Eq. (15) (thus, only a face-normal component is used) for the $M_\infty = 0.6$ case to investigate their effects. The computed flowfields are shown in Fig. 20. This figure reveals that the use of a multidimensional Mach number in Eq. (15) is necessary instead of the cell-interface normal Mach number, as mentioned earlier.

L. Viscous Flow over Flat Plate (Moderate Mach Number, Viscous)

As in [25], $M_\infty = 0.2$ viscous flow over a flat plate is solved by using different flux functions, along with MUSCL without a limiter, and the second-order Runge–Kutta method (Fig. 21). The viscous term is given by a conventional second-order central difference. Computations are conducted for 50,000 time steps with CFL = 0.5, which achieved three orders of density-residual reduction. The inflow boundary is placed a 4% plate length ahead, and the freestream condition is imposed with Riemann invariants conserved;

Table 3 Comparison of Strouhal number of vortex shedding by SLAU and the Roe scheme using several meshes

Scheme	SLAU			Roe		Experiment [24]
Mesh (radial × azimuthal, stretching ratio)	100 × 100, 1.076	150 × 200, 1.047	300 × 400, 1.020	100 × 100, 1.076	150 × 200, 1.047	——
Strouhal no.	0.1616	0.1636	0.1639	——	0.1552	0.16

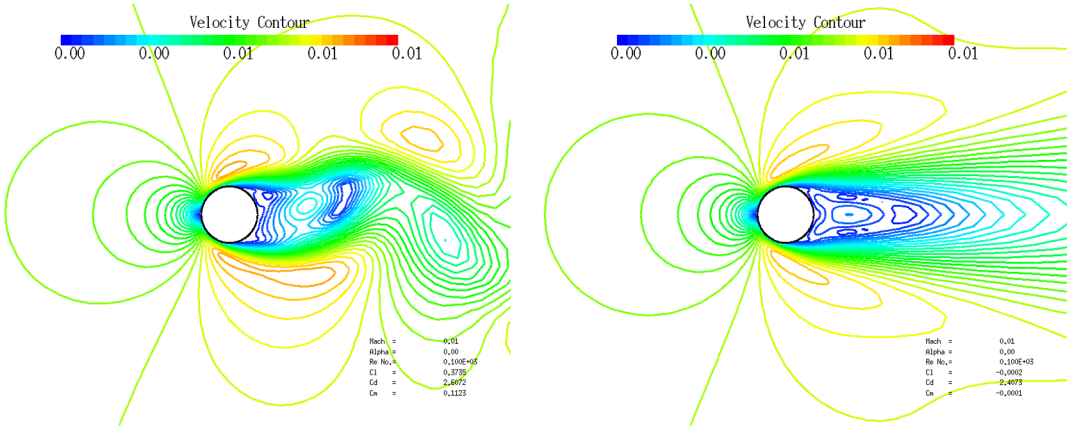

a) b)

Fig. 14 Velocity contours of flows around cylinder at $M = 0.01$ computed by a) SLAU and b) Roe schemes using coarse (100 × 100) mesh.

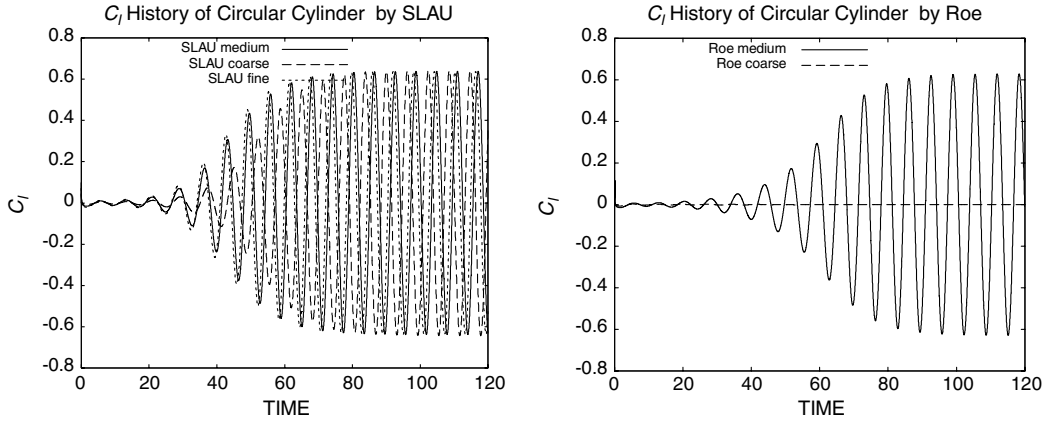

a) b)

Fig. 15 Time histories of lift coefficient of cylinder: a) SLAU and b) Roe.

all the primitive variables are extrapolated at the outflow and upper boundaries except for pressure, which is fixed as freestream value. As for the bottom boundary, the nonslip wall condition is employed at the plate and the slip condition at its upstream. The grid has 60×40 cells in flow and wall-normal directions, respectively (all the runs used the same grid). The grid spacing near the wall is $1.e-5$ plate length, and it is stretched upward with the ratio of 1.2. The wall condition starts from $i = 11$ at the bottom boundary, and velocity profiles are extracted along the $i = 31$ line where the Reynolds number based on the distance from the leading edge is $Re = 2.7e+4$. The results show that SLAU well reproduced Blasius' analytical velocity profile as the Roe flux.

M. Turbulent, Transonic Flow over NACA0012 Airfoil (Moderate Mach Number, Turbulent)

Finally, a transonic flow around the NACA0012 airfoil has been calculated again but with a different condition: $M_\infty = 0.703$,

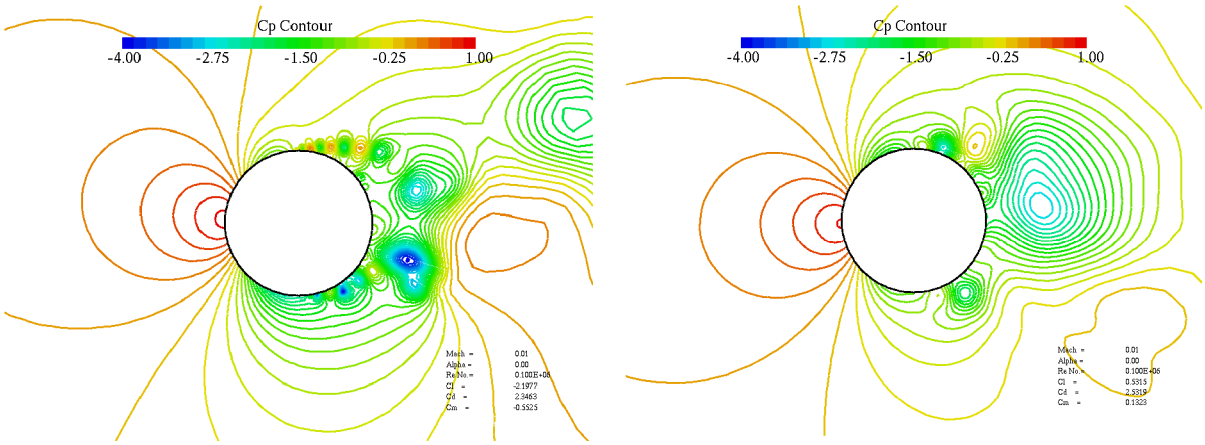

a) b)

Fig. 16 Pressure contours around cylinder in inviscid flow at $M_\infty = 0.01$ computed by a) SLAU and b) Roe.

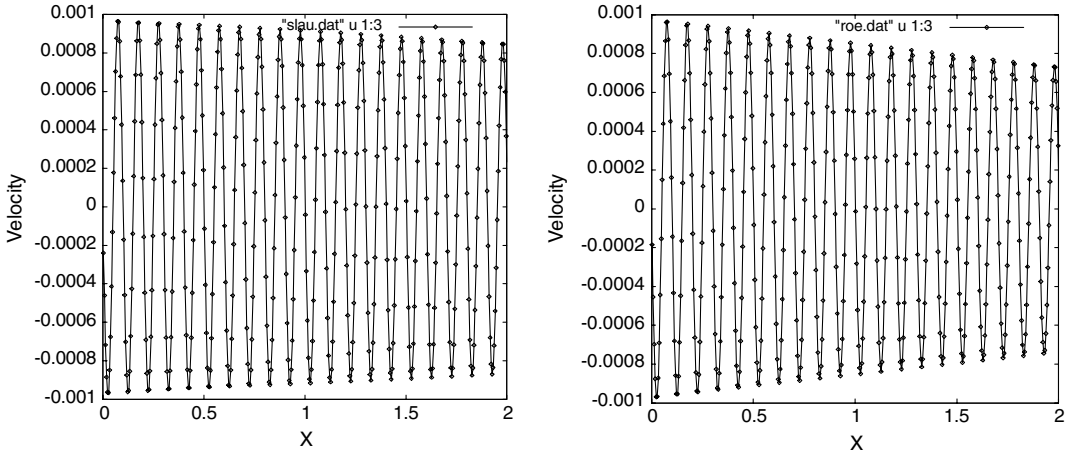

a) b)

Fig. 17 Velocity profile in 1-D sound propagation computed by a) SLAU and b) Roe.

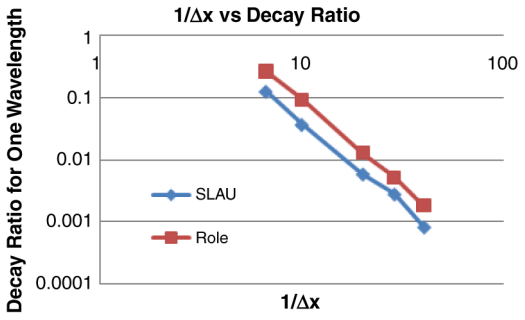

Fig. 18 Decay ratio per wavelength (ε/l) vs $l/\Delta x$.

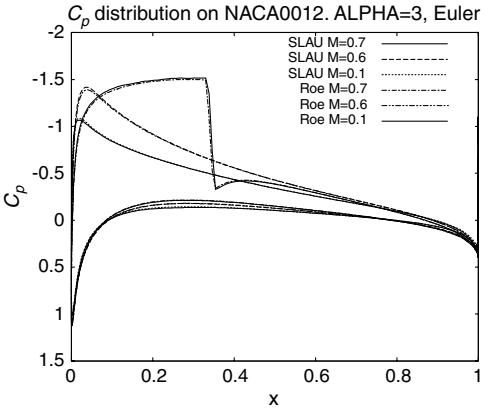

Fig. 19 Pressure profiles on NACA0012 airfoil of Euler solutions at various Mach numbers computed using SLAU and Roe schemes. Results by both schemes are very close.

$\alpha = 3.22°$, and $Re = 3.75 \times 10^6$, following [26]. This test is chosen to see viscous effects in a practical case involving a shock and a turbulent boundary-layer. SLAU, Roe, and AUSM+ are employed for calculation of the inviscid term. The Green–Gauss formula [27] is used for second-order spatial reconstruction coupled with Venkatakrishnan's limiter [28] with Wang's correction ($\varepsilon' = 0.05$) [29]. The Baldwin–Lomax [30] model is used with Wang's viscous term [11]. Computations are conducted with CFL = 20 (three inner iterations) for 10,000 time steps. The computational grid is O type having 200 (circumferential) × 100 (wall normal) cells, and the minimum spacing near the wall is 5.e − 6 chord length with the stretching ratio 1.1 outward. The outer boundary is 20 times the chord length away, and the aforementioned freestream condition is prescribed; the nonslip condition is used at the wall.

Figure 22 shows the typical computed flowfield and surface pressure coefficient profiles. The results by SLAU, Roe, and AUSM+ are very similar, including the shock profiles. In other words, at a moderate Mach number, SLAU shows a comparable

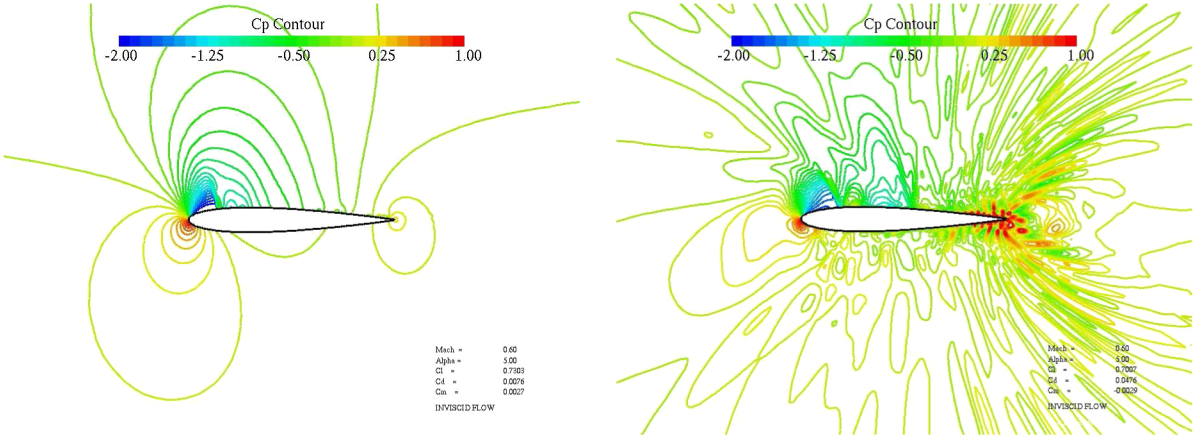

a) b)

Fig. 20 Comparison of pressure contour of Mach 0.6 flow around NACA0012 airfoil: a) SLAU and b) SLAU using normal Mach number in modification of pressure term in momentum equation.

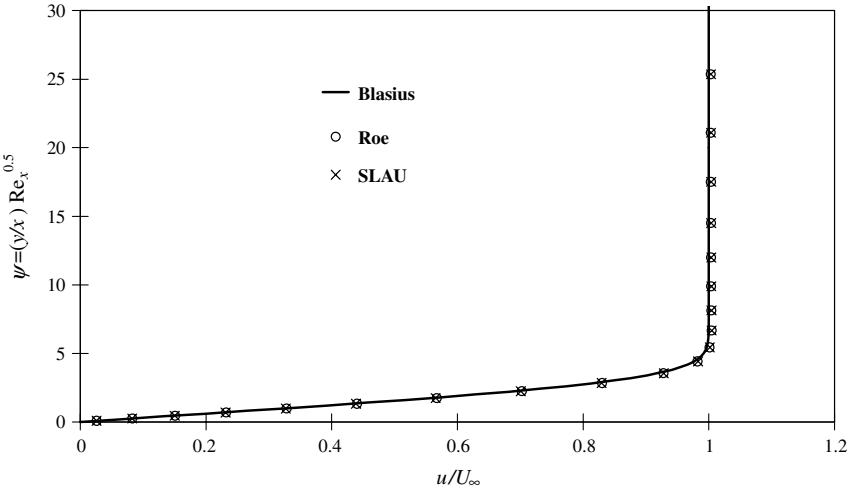

Fig. 21 Resolving boundary layer over flat plate (result of Roe taken from [25]).

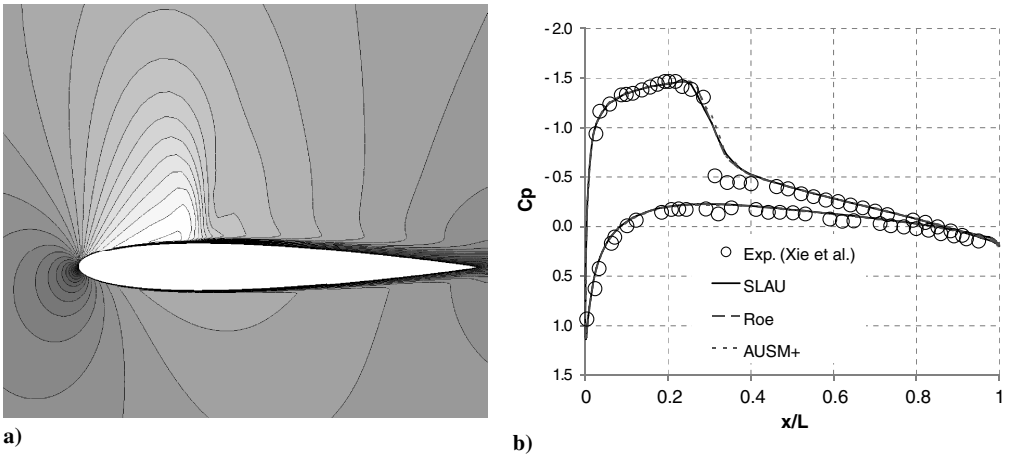

Fig. 22 Results for NACA0012 airfoil at $M_\infty = 0.85, \alpha = 1.25$ deg, and $Re_\infty = 3.75 \times 10^6$: a) Mach number contours (SLAU) and b) pressure profiles.

performance to well-known schemes such as Roe and AUSM+, even with shocks and turbulent effects.

IV. Conclusions

A new, parameter-free simple compressible numerical flux function of the AUSM family for all speeds, named SLAU, is presented. Although no tunable parameters (e.g., cutoff Mach number or reference velocity) are needed, SLAU is accurate, robust, and efficient for computations of wide-ranging Mach numbers. It hardly encounters shock anomalies, such as the carbuncle phenomena at high speeds, while it exhibits low numerical dissipation at low speeds.

The overall present strategy for construction of the scheme is summarized as follows: 1) use of AUSM-type formulation, 2) modification of the pressure term in the momentum equation for low dissipation, 3) activation of the pressure difference term in the mass flux function at low Mach numbers, 4) designing the pressure term in the mass flux to suppress shock anomalies at high Mach numbers, and 5) use of a common expression for the pressure function and multidimensional Mach number term.

In particular, by using multidimensional velocity components rather than only a face-normal one, SLAU eliminated the need of a cutoff Mach number required in other all-speed schemes. Thus, SLAU can be applied to any low Mach numbers without any adjustments depending on problems. This is desirable in internal flow simulations where no uniform flow is properly defined. Furthermore, the multidimensional term can readily be extended to unstructured grids.

Then, numerical tests demonstrated the following features of SLAU: 1) robustness against the known pathological behaviors in hypersonic flows; 2) low dissipation and a wide applicability, including aeroacoustics at low speeds; 3) dramatically accelerated convergence in combination with time-derivative preconditioning at a very low Mach number (although no parameters are derived from the preconditioning matrix); and 4) performances at moderate speeds comparable with well-known schemes such as Roe and AUSM+, even with viscous effects.

All in all, SLAU is promising, because it exhibits no severe problems from a low speed to a moderately supersonic speed, and it hardly does in a hypersonic flow. SLAU is simpler than existing all-speed AUSM-family schemes and involves no tunable parameters; hence, it can easily be coded and extended for complex physics, such as multispecies and multiphase flows.

Appendix A: Formulation of Simple Low-Dissipation Advection Upstream Splitting Method

The numerical flux of the AUSM-family scheme including SLAU is written as

$$\tilde{\mathbf{F}} = \frac{\dot{m} + |\dot{m}|}{2}\boldsymbol{\Phi}^+ + \frac{\dot{m} - |\dot{m}|}{2}\boldsymbol{\Phi}^- + \tilde{p}\mathbf{N} \tag{A1}$$

$$\boldsymbol{\Phi} = (1, u, v, w, h)^T \tag{A2}$$

$$\mathbf{N} = (0, x_n, y_n, z_n, 0)^T \tag{A3}$$

$$h = (e + p)/\rho \tag{A4}$$

The mass flux function of SLAU is given by

$$\dot{m} = \frac{1}{2}\{(\rho V_n)^+ + (\rho V_n)^- - |\bar{V}_n|\Delta\rho\}(1 - g) - \frac{\chi}{2\bar{c}}\Delta p \tag{A5}$$

$$\chi = (1 - \widehat{M})^2 \tag{A6}$$

$$\widehat{M} = \min\left(1.0, \frac{1}{\bar{c}}\sqrt{\frac{u^{+2} + v^{+2} + w^{+2} + u^{-2} + v^{-2} + w^{-2}}{2}}\right) \tag{A7}$$

$$|\bar{V}_n| = \frac{\rho^+|V_n|^+ + \rho^-|V_n|^-}{\rho^+ + \rho^-} \tag{A8}$$

$$g = -\max[\min(M^+, 0), -1] \cdot \min[\max(M^-, 0), 1] \quad \in [0, 1] \tag{A9}$$

$$M^\pm = \frac{V_n^\pm}{\bar{c}} = \frac{u^\pm x_n + v^\pm y_n + w^\pm z_n}{\bar{c}} \tag{A10}$$

$$\bar{c} = (c^+ + c^-)/2 \tag{A11}$$

Finally, the pressure function is given by

$$\tilde{p} = \frac{p^+ + p^-}{2} + \frac{\beta_+ - \beta_-}{2}(p^+ - p^-) + (1 - \chi)(\beta_+ + \beta_- - 1)\frac{p^+ + p^-}{2} \tag{A12}$$

$$\beta_\pm = \begin{cases} \frac{1}{4}(2 \mp M^\pm)(M^\pm \pm 1)^2 & \text{for } |M^\pm| < 1 \\ \frac{1}{2}[1 + \text{sign}(\pm M^\pm)] & \text{otherwise} \end{cases} \tag{A13}$$

Appendix B: Formulation of AUSM$^+$-up

For comparison, the formulation of AUSM$^+$-up is reviewed. The general expression is common to the one in SLAU:

$$\tilde{\mathbf{F}} = \frac{\dot{m} + |\dot{m}|}{2}\boldsymbol{\Phi}^+ + \frac{\dot{m} - |\dot{m}|}{2}\boldsymbol{\Phi}^- + \tilde{p}\mathbf{N} \tag{B1}$$

$$\boldsymbol{\Phi} = (1, u, v, w, h)^T \tag{B2}$$

$$\mathbf{N} = (0, x_n, y_n, z_n, 0)^T \tag{B3}$$

$$h = (e + p)/\rho \tag{B4}$$

The mass flux, pressure flux, and other functions are written as follows:

$$\dot{m} = M_{1/2}c_{1/2}\begin{cases} \rho_L & \text{if } M_{1/2} > 0 \\ \rho_R & \text{otherwise} \end{cases}\text{: mass flux} \tag{B5}$$

$$M_{1/2} = f_M^+ + f_M^- + M_p \tag{B6}$$

$$f_M^\pm = \begin{cases} \frac{1}{2}(M \pm |M|), & \text{if } |M| \geq 1 \\ \pm\frac{1}{4}(M \pm 1)^2 \pm \frac{1}{8}(M^2 - 1)^2, & \text{otherwise} \end{cases} \tag{B7}$$

$$M_p = -\frac{K_p}{f_a}\max(1 - \sigma\bar{M}^2, 0)\frac{p_R - p_L}{\rho_{1/2}c_{1/2}^2}, \qquad \rho_{1/2} = \frac{\rho_L + \rho_R}{2} \tag{B8}$$

$$\tilde{p} = \beta_+|_\alpha p_L + \beta_-|_\alpha p_R + p_u\text{: pressure flux} \tag{B9}$$

$$\beta_\pm|_\alpha = \begin{cases} \frac{1}{2}[1 \pm \text{sign}(M)], & \text{if } |M| \geq 1 \\ \frac{1}{4}(M \pm 1)^2(2 \mp M) \pm \alpha M(M^2 - 1)^2, & \text{otherwise} \end{cases} \tag{B10}$$

$$p_u = -K_u\beta_+\beta_-(\rho_L + \rho_R)(f_a c_{1/2})(V_n^- - V_n^+) \tag{B11}$$

$$c_{1/2} = \min(\tilde{c}_L, \tilde{c}_R), \qquad \tilde{c}_L = c^{*2}/\max(c^*, V_n^+) \qquad \tilde{c}_R = c^{*2}/\max(c^*, -V_n^-) \tag{B12}$$

$$c^{*2} = \frac{2(\gamma - 1)}{(\gamma + 1)}h \tag{B13}$$

$$\alpha = \frac{3}{16}(-4 + 5f_a^2) \tag{B14}$$

$$f_a(M_o) = M_o(2 - M_o) \tag{B15}$$

$$M_o^2 = \min[1, \max(\bar{M}^2, M_\infty^2)] \tag{B16}$$

$$\bar{M}^2 = \frac{V_n^{+2} + V_n^{-2}}{2c_{1/2}^2} \tag{B17}$$

with the following parameters:

$$K_p = 0.25, \qquad K_u = 0.75, \qquad \sigma = 1.0 \tag{B18}$$

Appendix C: Formulation of AUSM+

The formulation of AUSM+ is reviewed. Again, the general expression is common to the one in SLAU:

$$\tilde{\mathbf{F}} = \frac{\dot{m} + |\dot{m}|}{2}\boldsymbol{\Phi}^+ + \frac{\dot{m} - |\dot{m}|}{2}\boldsymbol{\Phi}^- + \tilde{p}\mathbf{N} \tag{C1}$$

$$\boldsymbol{\Phi} = (1, u, v, w, h)^T \tag{C2}$$

$$\mathbf{N} = (0, x_n, y_n, z_n, 0)^T \tag{C3}$$

$$h = (e + p)/\rho \tag{C4}$$

The mass flux, pressure flux, and other functions are written as follows:

$$\dot{m} = M_{1/2}c_{1/2}\begin{cases} \rho_L & \text{if } M_{1/2} > 0 \\ \rho_R & \text{otherwise} \end{cases}\text{: mass flux} \tag{C5}$$

$$M_{1/2} = f_M^+ + f_M^- \tag{C6}$$

$$f_M^\pm = \begin{cases} \frac{1}{2}(M \pm |M|), & \text{if } |M| \geq 1 \\ \pm\frac{1}{4}(M \pm 1)^2 \pm \frac{1}{8}(M^2 - 1)^2, & \text{otherwise} \end{cases} \tag{C7}$$

$$\tilde{p} = \beta_+|_{\alpha=3/16}p_L + \beta_-|_{\alpha=3/16}p_R\text{: pressure flux} \tag{C8}$$

$$\beta_{\pm}|_{\alpha} = \begin{cases} \frac{1}{2}(1 \pm \text{sign}(M)), & \text{if } |M| \geq 1 \\ \frac{1}{4}(M \pm 1)^2(2 \mp M) \pm \alpha M(M^2-1)^2, & \text{otherwise} \end{cases} \tag{C9}$$

$$c_{1/2} = \min(\tilde{c}_L, \tilde{c}_R), \qquad \tilde{c}_{L/R} = c^{*2}/\max(c^*, |V_n^{\pm}|) \tag{C10}$$

$$c^{*2} = \frac{2(\gamma-1)}{(\gamma+1)}h \tag{C11}$$

Appendix D: Weiss and Smith Preconditioning Matrix

The preconditioning matrix of Weiss and Smith [1] is described as follows:

$$\Gamma^{-1} = \mathbf{I} - \frac{(1-\varepsilon)(\gamma-1)}{c^2} \cdot \text{diag}(1, \quad u, \quad v, \quad w, \quad H) \cdot \begin{pmatrix} \frac{q^2}{2} & -u & -v & -w & 1 \\ \frac{q^2}{2} & -u & -v & -w & 1 \\ \frac{q^2}{2} & -u & -v & -w & 1 \\ \frac{q^2}{2} & -u & -v & -w & 1 \\ \frac{q^2}{2} & -u & -v & -w & 1 \end{pmatrix} \tag{D1}$$

$$\varepsilon = \min[1, \max(KM^2, M_{\text{co}}^2)] \tag{D2}$$

$$q^2 = u^2 + v^2 + w^2 \tag{D3}$$

where K is constant, usually taken as 0.25–1.0 ($K = 1.0$ is chosen in this work), and M_{co} is the cutoff Mach number, which is as the same order as freestream Mach number M_{∞}.

Appendix E: Formulation of Preconditioned Matrix Free Gauss–Seidel and Lower–Upper Symmetric Gauss–Seidel with Preconditioning

Navier–Stokes equations for viscous compressible flow can be written in the finite volume form, including the local preconditioning matrix as follows:

$$\frac{V_i}{\Delta t_i}\Delta\mathbf{Q}_i + \Gamma_i^{-1}\sum_j(\tilde{\mathbf{F}}_{i,j} - \tilde{\mathbf{R}}_{i,j})s_{i,j} = 0 \tag{E1}$$

$$\Delta\mathbf{Q}_i = \mathbf{Q}_i^{n+1} - \mathbf{Q}_i^n \tag{E2}$$

where $\mathbf{Q}_i$ are the vectors of the conservative variables of cell i; $\tilde{\mathbf{F}}_{i,j}$ and $\tilde{\mathbf{R}}_{i,j}$ are the inviscid and viscous fluxes normal to the cell face from the cell i to one of its surrounding cells j; $s_{i,j}$ is the area of the cell interface of i and j; and Γ_i^{-1} is the local preconditioning matrix.

The Euler implicit time integration can be written with introducing approximation using linearization and first-order upwinding in the right-hand side as

$$\left(\frac{V_i}{\Delta t_i}\mathbf{I} + \sum_j s_{i,j}\Gamma_i^{-1}\tilde{\mathbf{A}}_{i,j}^{+}\right)\Delta\mathbf{Q}_i - \sum_j s_{i,j}\Gamma_i^{-1}\tilde{\mathbf{A}}_{j,i}^{+}\Delta\mathbf{Q}_j = -\Gamma_i^{-1}\sum_j(\tilde{\mathbf{F}}_{i,j} - \tilde{\mathbf{R}}_{i,j})s_{i,j} \tag{E3}$$

$$\tilde{\mathbf{A}}_{i,j}^{+} = \frac{|\tilde{\mathbf{A}}|_{i,j} + \tilde{\mathbf{A}}_{i,j}}{2} \tag{E4}$$

$$\tilde{\mathbf{A}}_{i,j} = \frac{\partial\tilde{\mathbf{F}}_{i,j}}{\partial\mathbf{Q}} - \frac{\partial\tilde{\mathbf{R}}_{i,j}}{\partial\mathbf{Q}} \tag{E5}$$

where $|\mathbf{A}|$ is a matrix in which eigenvalues are replaced by their absolute values of Jacobian matrix $\mathbf{A}$. According to the diagonal dominance of the system, we can use the Gauss–Seidel iteration to solve this linear system as

$$\Delta\mathbf{Q}_i^{\text{new}} = \left(\frac{V_i}{\Delta t_i}\mathbf{I} + \sum_j s_{i,j}\Gamma_i^{-1}\tilde{\mathbf{A}}_{i,j}^{+}\right)^{-1}\Gamma_i^{-1}\left\{\sum s_{i,j}\tilde{\mathbf{A}}_{j,i}^{+}\Delta\mathbf{Q}_j^{\text{recent}} - \sum_j(\tilde{\mathbf{F}}_{i,j} - \tilde{\mathbf{R}}_{i,j})s_{i,j}\right\} \tag{E6}$$

The approximate Jacobian matrix proposed by Jameson and Turkel [19] is introduced for simplification as

$$(\Gamma_i^{-1}\tilde{\mathbf{A}}_{i,j})^{+} \approx \frac{\Gamma_i^{-1}\tilde{\mathbf{A}}_{i,j} + \sigma_{i,j}\mathbf{I}}{2} \tag{E7}$$

Here, σ is the spectral radius using variables at cell i, in the direction from i to j, defined by the following equation by applying the preconditioning matrix of Weiss and Smith [1] and adding the viscous term,

$$\sigma_{i,j} = \frac{1}{2}\{(1+\varepsilon)|V_{ni,j}| + \sqrt{(\varepsilon-1)^2V_{ni,j}^2 + 4\varepsilon c_i^2}\} + \frac{2(\mu+\mu_T)s_{i,j}}{\rho_i V_i} \tag{E8}$$

with the parameter ε to control numerical sound of speed. Here, ε is defined as

$$\varepsilon = \min[1, \max(M^2, M_{\text{cutoff}}^2)] \tag{E9}$$

By using this approximation, the multiplication of the block matrix in Eq. (E6) is simplified to a scalar division:

$$\Delta\mathbf{Q}_i^{\text{new}} = \Gamma_i^{-1}\left\{\sum s_{i,j}\tilde{\mathbf{A}}_{j,i}^{+}\Delta\mathbf{Q}_j^{\text{recent}} - \sum_j(\tilde{\mathbf{F}}_{i,j} - \tilde{\mathbf{R}}_{i,j})s_{i,j}\right\} \Big/ \left(\frac{V_i}{\Delta t_i} + \frac{1}{2}\sum_j s_{i,j}\sigma_{i,j}\right) \because \sum_j s_{i,j}\tilde{\mathbf{A}}_{i,j} = 0 \tag{E10}$$

Other matrix operations are also simplified using the reverse linearization,

$$(\Gamma_i^{-1}\tilde{\mathbf{A}}_{j,i})^{+}\Delta\mathbf{Q}_j \approx \frac{\Gamma_i^{-1}\tilde{\mathbf{A}}_{j,i} + \sigma_{j,i}I}{2}\Delta\mathbf{Q}_j \approx \frac{\Gamma_i^{-1}(\hat{\mathbf{F}}_{j,i}(\mathbf{Q}_j^n + \Delta\mathbf{Q}_j) - \hat{\mathbf{F}}_{j,i}(\mathbf{Q}_j^n)) + \sigma_{j,i}\Delta\mathbf{Q}_j}{2} \tag{E11}$$

$$\hat{\mathbf{F}}_{j,i} = \begin{pmatrix} \rho V_n \\ \rho u V_n + p x_n \\ \rho v V_n + p y_n \\ \rho w V_n + p z_n \\ (e+p)V_n \end{pmatrix} \tag{E12}$$

I. Preconditioned Matrix Free Gauss–Seidel

The summation of the matrix multiplication in Eq. (E10) is further simplified, changing the position of variable. Be careful to the change between the second line and the third line in the following equation:

$$\sum_j s_{i,j}(\Gamma_i^{-1}\tilde{\mathbf{A}}_{j,i})^+\Delta\mathbf{Q}_j$$
$$\approx \sum_j s_{i,j}\frac{\Gamma_i^{-1}[\hat{\mathbf{F}}_{j,i}(\mathbf{Q}_j^n+\Delta Q_j)-\hat{\mathbf{F}}_{j,i}(\mathbf{Q}_j^n)]+\sigma_{j,i}\Delta\mathbf{Q}_j}{2}$$
$$\approx \sum_j s_{i,j}\frac{\Gamma_i^{-1}[\hat{\mathbf{F}}_{j,i}(\mathbf{Q}_i^n+\Delta\mathbf{Q}_j)-\hat{\mathbf{F}}_{j,i}(\mathbf{Q}_i^n)]+\sigma_{i,j}\Delta\mathbf{Q}_j}{2}$$
$$=\Gamma_i^{-1}\sum_j s_{i,j}\frac{\hat{\mathbf{F}}_{j,i}(\mathbf{Q}_i^n+\Delta\mathbf{Q}_j)}{2}$$
$$+\sum_j s_{i,j}\frac{\sigma_{i,j}\Delta\mathbf{Q}_j}{2}\because\sum_j s_{i,j}\hat{\mathbf{F}}_{j,i}(\mathbf{Q}_i^n)=-\sum_j s_{i,j}\hat{\mathbf{F}}_{i,j}(\mathbf{Q}_i^n)=0 \quad \text{(E13)}$$

Finally, the Gauss–Seidel iteration that contains no block matrix operation, named the preconditioned MFGS (PMFGS) scheme, is defined as

$$\Delta\mathbf{Q}_i^{\text{new}}=\left[\Gamma_i^{-1}\left\{\sum_j s_{i,j}\frac{\hat{\mathbf{F}}_{j,i}(\mathbf{Q}_i^n+\Delta\mathbf{Q}_j)}{2}-\sum_j s_{i,j}(\hat{\mathbf{F}}_{i,j}-\tilde{\mathbf{R}}_{i,j})\right\}+\sum_j s_{i,j}\frac{\sigma_{i,j}\Delta\mathbf{Q}_j}{2}\right]\Bigg/\left(\frac{V_i}{\Delta t_i}+\sum_j s_{i,j}\frac{\sigma_{i,j}}{2}\right) \quad \text{(E14)}$$

Note that Γ^{-1} becomes the identity matrix and PMFGS becomes the original MFGS [20] when ε is chosen to be unity. Also note that the multiplication of Γ^{-1} in Eq. (E14) turns to become the simple vector operation,

$$\Gamma_i^{-1}\delta\mathbf{Q}\equiv\delta\mathbf{Q}-\frac{(1-\varepsilon)\delta p}{c^2}(1,u,v,w,h)^T \quad \text{(E15)}$$

$$\delta p\equiv(\gamma-1)\left(\frac{u^2+v^2+w^2}{2}\delta\rho-u\delta\rho u-v\delta\rho v-w\delta\rho w+\delta e\right)$$

Thus, the increase of computational costs is small [1]. The order and number of sweeps are arbitrarily chosen in MFGS; however, symmetric sweeps are preferred for subsonic flows.

II. LU-SGS with Preconditioning

On the other hand, the LU-SGS scheme with the preconditioning matrix is written as follows:

Forward sweep:

$$\Delta\mathbf{Q}_i^*=\Gamma_i^{-1}\left\{\sum_{j\in\text{lower}}s_{i,j}\tilde{\mathbf{A}}_{j,i}^+\Delta\mathbf{Q}_j^*-\sum_j(\tilde{\mathbf{F}}_{i,j}-\tilde{\mathbf{R}}_{i,j})s_{i,j}\right\}\Bigg/\left(\frac{V_i}{\Delta t_i}+\sum_j s_{i,j}\frac{\sigma_{i,j}}{2}\right) \quad \text{(E16)}$$

Backward sweep:

$$\Delta\mathbf{Q}_i=\Delta\mathbf{Q}_i^*+\Gamma_i^{-1}\left(\sum_{j\in\text{upper}}s_{i,j}\tilde{\mathbf{A}}_{j,i}^+\Delta\mathbf{Q}_j\right)/\left(\frac{V_i}{\Delta t_i}+\sum_j s_{i,j}\frac{\sigma_{i,j}}{2}\right)$$

The reverse linearization defined by Eq. (E10) can be also used as well. Note that the approximation used in Eq. (E13) cannot be used in LU-SGS.

Acknowledgments

Taku Nonomura, of the Japan Aerospace Exploration Agency (JAXA), kindly reviewed the draft of the paper and gave the authors a valuable suggestion. Seiji Tsutsumi, at JAXA's Engineering Digital Innovation (JEDI) center, and Nobuyuki Tsuboi, at the Kyushu Institute of Technology, provided the authors with helpful information. The unstructured grid solver LS-FLOW, used in the turbulent airfoil case, was developed by Keiichiro Fujimoto and Kazuto Kuzuu with the authors at JEDI center. The authors are grateful for all their support.

References

[1] Weiss, J. M., and Smith, W. A., "Preconditioning Applied to Variable and Constant Density Flows," *AIAA Journal*, Vol. 33, No. 11, 1995, pp. 2050–2057. doi:10.2514/3.12946

[2] Turkel, E., "Preconditioning Technique in Computational Fluid Dynamics," *Annual Review of Fluid Mechanics*, Vol. 31, 1999, pp. 385–416. doi:10.1146/annurev.fluid.31.1.385

[3] Unrau, D., and Zingg, D. W., "Viscous Airfoil Computations Using Local Preconditioning," AIAA Paper 1997-2027, 1997.

[4] Li, X. S., and Gu, C. W., "An All-Speed Roe-Type Scheme and Its Asymptotic Analysis of Low Mach Number Behavior," *Journal of Computational Physics*, Vol. 227, No. 10, 2008, pp. 5144–5159. doi:10.1016/j.jcp.2008.01.037

[5] Liou, M. S., and Steffen, C. J., Jr., "A New Flux Splitting Scheme," *Journal of Computational Physics*, Vol. 107, No. 1, 1993, pp. 23–39. doi:10.1006/jcph.1993.1122

[6] Liou, M. S., "A Sequel to AUSM: AUSM$^+$," *Journal of Computational Physics*, Vol. 129, No. 2, 1996, pp. 364–382. doi:10.1006/jcph.1996.0256

[7] Wada, Y., and Liou, M. S., "An Accurate and Robust Flux Splitting Scheme for Shock and Contact Discontinuities," *SIAM Journal on Scientific Computing*, Vol. 18, No. 3, 1997, pp. 633–657. doi:10.1137/S1064827595287626

[8] Shima, E., "Role of CFD in Aeronautical Engineering (No. 14): AUSM Type Upwind Schemes," *Proceedings of 13th NAL Symposium on Aircraft Computational Aerodynamics*, SP30, National Aerospace Lab., Tokyo, 1996, pp. 41–46.

[9] Edwards, J. R., "Towards Unified CFD Simulation of Real Fluid Flows," AIAA Paper 2001-2524, 2001.

[10] Liou, M. S., "A Sequel to AUSM, Part II: AUSM$^+$-up for All Speeds," *Journal of Computational Physics*, Vol. 214, No. 1, 2006, pp. 137–170. doi:10.1016/j.jcp.2005.09.020

[11] Wang, Z. J., "A Quadtree-based Adaptive Cartesian/Quad Grid Flow Solver for Navier–Stokes Equations," *Computers and Fluids*, Vol. 27, No. 4, 1998, pp. 529–549. doi:10.1016/S0045-7930(97)00070-4

[12] Van Leer, B., "Flux Vector Splitting for the Euler Equations," *Lecture Notes in Physics*, Vol. 170, 1982, pp. 507–512. doi:10.1007/3-540-11948-5_66

[13] Liou, M. S., "Mass Flux Schemes and Connection to Shock Instability," *Journal of Computational Physics*, Vol. 160, No. 2, 2000, pp. 623–648. doi:10.1006/jcph.2000.6478

[14] Shima, E., Nagata, T., and Ochi, A., "Analysis of High Lift Configuration Using Unstructured Overset Mesh and Improved SHUS," *Proceedings of 20th CFD Symposium of JSFM* [CD-ROM], Japan Soc. of Fluid Mechanics, Tokyo, 2006 (in Japanese).

[15] Kitamura, K., Roe, P., and Ismail, F., "Evaluation of Euler Fluxes for Hypersonic Flow Computations," *AIAA Journal*, Vol. 47, No. 1, 2009, pp. 44–53. doi:10.2514/1.33735

[16] Quirk, J. J., "A Contribution to the Great Riemann Solver Debate," *International Journal for Numerical Methods in Fluids*, Vol. 18, No. 6, 1994, pp. 555–574. doi:10.1002/fld.1650180603

[17] Kitamura, K., Fujimoto, K., Shima, E., and Wang, Z. J., "Performance of Low-Dissipation Euler Fluxes and Preconditioned LU-SGS at Low Speeds," *Communications in Computational Physics*, Vol. 10, 2011, pp. 90–119. doi:10.4208/cicp.041109.160910a

[18] Roe, P. L., "Approximate Riemann Solvers, Parameter Vectors, and Difference Schemes," *Journal of Computational Physics*, Vol. 43, No. 2, 1981, pp. 357–372. doi:10.1016/0021-9991(81)90128-5

[19] Jameson, A., and Turkel, E., "Implicit Schemes and LU Decompositions," *Mathematics of Computation*, Vol. 37, No. 156, 1981, pp. 385–397. doi:10.2307/2007433

[20] Shima, E., "A Simple Implicit Scheme for Structured/Unstructured CFD," *Proceedings of the 29th Fluid Dynamic Conference*, Japan Soc. for Aeronautical and Space Sciences, Tokyo, 1997, pp. 325–328 (in Japanese).

[21] Kitamura, K., Shima, E., Nakamura, Y., and Roe, P. L., "Evaluation of

Euler Fluxes for Hypersonic Heating Computations," *AIAA Journal*, Vol. 48, No. 4, 2010, pp. 763–776. doi:10.2514/1.41605

[22] van Albada, G. D., van Leer, B., and Roberts, W. W., Jr., "A Comparative Study of Computational Methods in Cosmic Gas Dynamics," *Astronomy and Astrophysics*, Vol. 108, No. 1, 1982, pp. 76–84.

[23] Ismail, F., and Roe, P. L., "Affordable, Entropy-Consistent Euler Flux Functions II: Entropy Production at Shocks," *Journal of Computational Physics*, Vol. 228, No. 15, 2009, pp. 5410–5436. doi:10.1016/j.jcp.2009.04.021

[24] Williamson, C. H. K., "Vortex Dynamics in the Wake of A Cylinder," *Fluid Vortex*, edited by S. I. Green, Kluwer Academic Publ., Dordrecht, The Netherlands, 1995, p. 177.

[25] Nishikawa, H., and Kitamura, K., "Very Simple, Carbuncle-Free, Boundary-Layer Resolving, Rotated-Hybrid Riemann Solvers," *Journal of Computational Physics*, Vol. 227, No. 4, 2008, pp. 2560–2581. doi:10.1016/j.jcp.2007.11.003

[26] Xie, F., Song, W., and Han, Z., "Numerical Study of High-Resolution Scheme Based on Preconditioning Method," *Journal of Aircraft*, Vol. 46, No. 2, 2009, pp. 520–525. doi:10.2514/1.37976

[27] Mavriplis, D. J., "Revisiting the Least-Squares Procedure for Gradient Reconstruction on Unstructured Meshes," AIAA Paper 2003-3986, 2003.

[28] Venkatakrishnan, V., "Convergence to Steady State Solutions of the Euler Equations on Unstructured Grids with Limiters," *Journal of Computational Physics*, Vol. 118, No. 1, 1995, pp. 120–130. doi:10.1006/jcph.1995.1084

[29] Wang, Z. J., "A Fast Nested Multi-Grid Viscous Flow Solver for Adaptive Cartesian/Quad Grids," *International Journal for Numerical Methods in Fluids*, Vol. 33, No. 5, 2000, pp. 657–680. doi:10.1002/1097-0363(20000715)33:5<657::AID-FLD24>3.0.CO;2-G

[30] Baldwin, B., and Lomax, H., "Thin Layer Approximation and Algebraic Model for Separated Turbulent Flows," AIAA Paper 1978-0257, 1978.

W. Anderson
Associate Editor